Characterization of a Wideband Monopulse Piezoelectric Direction Finder

by

PHILLIP JAMES ROWE

S.B. Electrical Science and Engineering
Massachusetts Institute of Technology (1997)

Submitted to the Department of Electrical Engineering and Computer Science
in partial fulfillment of the requirements for the degree of

Master of Engineering in Electrical Engineering and Computer Science

at the

MASSACHUSETTS INSTITUTE OF TECHNOLOGY

May 28, 1999

Author ....
Department of Electrical Engineering and Computer Science
May 28, 1999

Certified by ....
Joseph A. Paradiso
Principal Research Scientist
Thesis Supervisor

Accepted by ....
Arthur C. Smith
Chairman, Department Committee on Graduate Theses

Characterization of a Wideband Monopulse Piezoelectric Direction Finder

by

PHILLIP JAMES ROWE

Submitted to the Department of Electrical Engineering and Computer Science
on May 28, 1999, in partial fulfillment of the
requirements for the degree of
Master of Engineering in Electrical Engineering and Computer Science

Abstract

Sound localization has been the subject of much ongoing research in the area of beamformers and microphone arrays. Although these methods have been successful under certain conditions, the signal processing requirements needed for real-time operation are extensive.

This thesis describes the construction and test of a piezoelectric monopulse direction-finding sensor used to determine the angular location of a source within the plane of the sensor. The design of the sensor exploits spatially derivative-matched sensing apertures to eliminate angle ambiguities and frequency dependence of the monopulse ratio. The electronics front end and processing are very simple, consisting of averaging the sample-by-sample ratios of the rectified-and-smoothed outputs during their reverberation-free time period.

Several experiments are described with different inputs, and the sensor's operation is compared to theoretical and simulated behavior. Although the effects of the hexcell support on the spatial weighting of the sensor are not fully understood, it is shown that the sensor behaves as a dispersionless monopulse sensor for an angular range of ± 40° and a bandwidth of 4 kHz. It is also shown that the sensor does not, in its current form, produce adequate signal levels to be used as a speech localization device.

Thesis Supervisor: Joseph A. Paradiso
Title: Principal Research Scientist
Media Lab Physics and Media Group

Acknowledgments

To Joe Paradiso, my thesis supervisor, who very patiently and wisely directed me and encouraged me, even when I was frustrated and exhausted. To Andre Van Schyndel, who shared our enthusiasm for this thesis and provided invaluable advice, equipment, and support. To Shawn Burke, who suggested the current electrode shape of the monopulse sensor and served as a reference in numerous regards. Thanks to Kyung Park from AMP Sensors (now Measurement Specialists) for providing the patterned PVDF foils.

To Ari Benbasat, who willingly provided ample assistance in all phases of this project and deserves his reputation as the go-to guy. To Joe Pompei and Josh Strickon, who saved me enormous amounts of time by sharing equipment and know-how. To Craig Abler, who developed the original Labview virtual instruments.

To all the unnamed professors, students, and staff at the Media Lab who make the Lab a cooperative and creative environment.

And to my friends, to Tay Tay, and to my family, who provided the moral support for this task and so many others in the past. And, most of all, to the Man upstairs, who gave me the ability and gumption for everything I do.

Contents

List of Figures

Chapter 1

Introduction

1.1 Motivation

Digital microphone arrays and digital signal processing are increasingly successful in providing portable, untethered sound recording in noisy, reverberant, and changing environments [16]. Microphone arrays can also be used to track a moving sound source. The applications for tracking and recording systems are numerous. For instance, in teleconferencing systems, it is often desired that a camera be steered toward the person speaking. Also, with improvements in speech recognition, tracking and sound pickup systems could be a key part of new human-computer interfaces [22].

A limitation to the proliferation of microphone array systems is their computational complexity. To improve the spatial selectivity of a recording system, microphones must be added to the array and the sampling rate of the channels must be increased. Thus, the computation engine needed with microphone array systems must accommodate not only the increased channel count but also the increased data rate per channel. Despite the power of today's processors and computers, the complexity of the problem is not trivial.

The "backgammon" device that will be characterized in this project promises to be an intrinsically dispersionless monopulse receiver, hence has potential to be a cheap and simple solution to the direction-finding component of the sound capture problem explained in Chapter 2. Previous work on a design adapted for underwater [12] showed positive results, and a prototype has been built for use in air. Further, the concept of this receiver could be used in embedding arbitrary system function on a sensing surface for the dual purposes of tracking and low-noise recording [24].

1.2 Goals

The immediate goals of this thesis are to characterize the in-air transducer and to compare it to conventional microphone array systems. The results of the characterization will indicate what design issues could be addressed to improve the microphone's performance.

1.3 Outline of thesis

This is chapter one, the **Introduction**, which introduces the thesis subject matter, the goals, and the outline of this thesis.

Chapter two, **Background**,describes the theory and conventional practices in audio direction finding and sound capture systems.

Chapter three, **Monopulse Direction Finding and Spatially-Weighted Apertures**, introduces the theory of monopulse receivers and describes previous work done in applying monopulse concepts to sonar direction finding.

Chapter four, **Construction and Test**, describes our prototype's construction for use in air and its characterization.

Chapter five, **Simulations and Data Analysis**, includes simulations, acquired data, and the analysis of that data.

Chapter six, **Future Work and Applications**, makes recommendations based on the results.

Chapter 2

Background

2.1 Definition of problem

The problem of untethered sound recording is often broken into the two smaller problems of (1) finding the location of a sound source within a potentially noisy, reverberant environment and (2) pointing or tuning a spatially selective recording device toward the located source. There are other methods relying on the characterization of a room's transfer responses, but this division is particularly useful for teleconferencing systems, for which it is desired to aim not only an audio recording device but also a video camera at the pertinent speaker. In this chapter we will briefly introduce several methods for localization and also for spatially selective sound capture.

2.2 Localization problem

Brandstein [4] divides the solutions to the audio localization problem into three categories: (1) beamformers, (2) high-resolution spectral estimators, and (3) time delay of arrival (TDOA) estimators. Before delving into each of these methods, however, we should point out the difficulties in the problem at hand. Audio signals are in general broadband, their statistics change with time, and their statistics are not known a priori. Thus, optimizing a location system for a certain frequency band and for an assumed noise process is often not good enough.

2.2.1 Beamformers for localization

Beamformers determine the location of a source by maximizing the output of a scanning, directional acoustic beam or of multiple, stationary, similar-shaped beams. Beamformers require considerable digital processing of potentially dense transducer arrays. The method of this thesis, split-beam monopulse, is similar to a beamformer because two beams are compared; the difference is that two different-shaped beams are compared, and the bulk of the signal processing is embedded in the design of the sensor. For the purposes of this discussion, we will classify monopulse as a beamforming technique.

2.2.2 Spectral estimators for localization

In spectral estimator systems, vast amounts of data are collected from sensor arrays and correlation matrices are calculated to determine an optimal or most likely source location. Although typically more accurate than beamformers, these spectra estimator systems require substantial computational power, and they do not perform well for very noisy or reverberant environments or for environments in which the statistics of the signals change with time.

2.2.3 TDOA for localization

The time delay of arrival estimators are simple spectral estimators, using only two sensors in an array. The TDOA is the time difference between the arrivals of the source signal to the two sensors in the array. Theoretically, only three TDOA's are necessary to triangulate the location of the source. This method is advantageous because it is faster than the more complex spectral estimators and more accurate

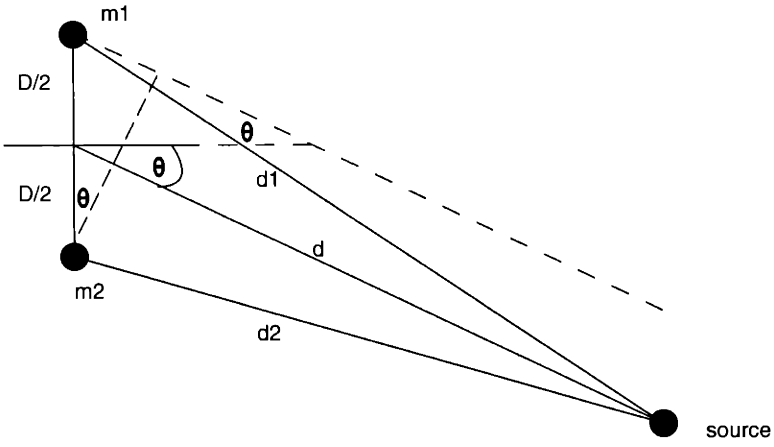

Figure 2-1: One source, two sensor model

than the simple beamformers [21].

Because the TDOA method is the simplified spectral estimator method, we will treat it in more depth here. Three methods for finding time delay estimates investigated by Omologo include (1) normalized cross correlation (NCC), (2) adaptive filtering, and (3) cross-power spectrum phase (CPSP) [18].

Signal Model

Assuming sound travels at velocity V_s and that our source is an ideal point source, the received signals for the microphone pair in Figure 2-1 are as follows:

$$r_i(t) = \alpha_i s(t - \frac{d_i}{V_s}) + e_i(t) \quad i = 1, 2 \tag{2.1}$$

The attenuation constant is inversely proportional to the distance from the source, and the noise is the sum of an interference component and a reverberation component.

$$e_i = e_{I,i}(t) + e_{R,i}(t) \tag{2.2}$$

Also, given the assumption that the spacing is much less than the distance to the source, the delay of arrival from one microphone to the next is proportional to the sine of the angle from normal.

$$t_1 - t_2 = \frac{d_1 - d_2}{V_s} \approx \frac{D}{V_s} sin\theta \quad if \quad D << d \tag{2.3}$$

Thus, finding the time delay of arrival indicates the direction of the source. Two TDOA estimates sufficiently describe a two-dimensional location, and three TDOA estimates provide a three-dimensional location.

Normalized Cross Correlation

The NCC in continuous time is defined as follows:

$$\hat{R}_{ij}^{(N)} = \frac{\int_{t-\frac{T}{2}}^{t+\frac{T}{2}} s_i(u) s_j(u+\tau) du}{\sqrt{\int_{t-\frac{T}{2}}^{t+\frac{T}{2}} s_i^2(u) du} \sqrt{\int_{t-\frac{T}{2}}^{t+\frac{T}{2}} s_j^2(u+\tau) du.}} \tag{2.4}$$

Continuous time is divided into a number of frames and for each frame the double-sided NCC is computed. The time delay having the highest NCC value is chosen as the TDOA for that frame. However, if the source $s(t)$ is periodic within the frame, the NCC shows several peaks. Thus, the maximum value within a frame may be offset by one or more periods from the actual TDOA.

Adaptive Filtering

A finite impulse response filter can be used to minimize the least-mean-square error between the two received signals by removing the delay. Ideally, only the FIR filter coefficient corresponding to the delay would be nonzero. To compensate for the time-varying noise characteristics, adaptive filters are implemented. Although this method works well, the next method works even better.

Cross-Power Spectrum Phase

The CPSP method is very similar to the NCC except that the signals are filtered before being correlated in order to generate a measurement that is independent of the spectrum characteristics of the signal. According to Omologo [18], the CPSP performed 20% better than adaptive filtering and 40% better than the NCC in simulations involving background noise, various sound sources, and an angle tolerance of five degrees. Thus, this is the preferred method for direction-finding using digital arrays.

Assuming that the time of flight between the source and sensors is an integer number of sampling points, we can write the signal model as follows [22], deriving a TDOA estimate every frame of N samples.

$$s_1[n] = s[n - M_1] \qquad M_i = (\frac{1}{T})\frac{d_i}{V_s} \tag{2.5}$$

$$s_2[n] = s[n - M_2] \qquad T = sampling \quad period \tag{2.6}$$

$$r_1[n] = \alpha_1 s_1[n] + e_1[n] \tag{2.7}$$

$$r_2[n] = \alpha_2 s_2[n] + e_2[n] \tag{2.8}$$

Forming a vector notation simplifies the representation of each frame.

$$\mathbf{s}_i[n] = s_i[n] \quad n = 0...(N-1) \tag{2.9}$$

$$\mathbf{s}_1[n] = s_1'[n] + v_1[n] \tag{2.10}$$

$$\mathbf{s}_2[n] = s_2'[n] + v_2[n] \tag{2.11}$$

$$v_i[n] = 0 \qquad if \quad n = M_i...(N-1), \tag{2.12}$$

$$= s(n - M_i) - s(n - M_i + N) \quad if \quad n = 0...M_{i-1} \tag{2.13}$$

$$\mathbf{r}_1[n] = \alpha_1 s_1'[n] + \alpha_1 v_1[n] + e_1[n] \tag{2.14}$$

$$\mathbf{r}_2[n] = \alpha_2 s_2'[n] + \alpha_2 v_2[n] + e_2[n] \tag{2.15}$$

From the time-shift property of the DFT,

$$\mathbf{s}[n] \longleftrightarrow \mathbf{S}[k] \tag{2.16}$$

$$\mathbf{s}\text{'}[n] \longleftrightarrow \mathbf{W}_N^{kM_i}\mathbf{S}[k] \tag{2.17}$$

The expression for the CPSP and the time delay estimate are as follows,

$$\begin{aligned} \mathbf{W}_N &= e^{\frac{-2j\pi}{N}} && (2.18) \\ CPSP &= IDFT(\frac{\mathbf{R}_1\mathbf{R}_2^*}{|\mathbf{R}_1|\,|\mathbf{R}_2|}) && (2.19) \\ M_{TDOA} &= n : max_n CPSP[n] && (2.20) \end{aligned}$$

and assuming the noise and interference is negligible, the M_{TDOA} is the inverse DFT of an exponential, which is equal to a time-delayed unit sample. In this case, the M_{TDOA} is unambiguously the offset from zero of the sample.

In practical settings, noise and interference levels are not negligible, and error in the TDOA estimates propagate to the location estimates. However, the accuracy of location estimates can be improved by using more than three TDOA estimates and eliminating those that correspond to smooth CPSP functions, which indicate ambiguity in the value of delay [22].

A low-cost, real-time system was built at the Center for Computer Aids for Industrial Productivity at Rutgers University. The system used a PC as the computation engine for determining location from the TDOA estimates. In a conference room, the system responded in 2 seconds by steering a camera to a speaker talking at a normal level. The system always pointed to a location within 30cm of the speaker's location. The system did not work well in an auditorium, however, where the reverberation levels were much higher.

2.3 Spatially selective sound capture

Two approaches to spatially selective sound capture that apply to microphone arrays and that will be described here are beamforming and matched filter array processing (MFA).

2.3.1 Beamforming

Beamforming [25] consists of the delay and summing of signals from an array of sensors such that the aggregate output of the array is directional. The resulting beam can be steered electronically by varying the delays in the summing paths, thus allowing the array itself to remain stationary. Also, multiple beams can be formed simultaneously with the same array, provided adequate processing power. This method is vulnerable to reverberant environments, however, because the signal to noise ratio decreases steadily with the number of reflections [23].

Another application that is inspired by work [13] done at Draper Laboratory in Cambridge, Massachuesetts, is the use of a continuous array to embed system functions onto a sensing surface. Applications include embedding arbitrary system functions onto surfaces for structural control [11] or SNR improvement [24]. This will be treated in depth in Chapter 3.

2.3.2 Matched filtering method

The MFA method can be used successfully in rooms with higher reverberation levels than beamformers, and it can be used to resolve a specific location in 3-space[23]. The method requires the knowledge of the transfer functions for every location to be resolved in the room. Because of the high degree of accuracy of the MFA method, a large number of transfer functions must be pre-determined, even for a small room. Renomeron et al. found the focal region of a system employing the MFA technique to be less than 20cm [23].

Chapter 3

Monopulse Direction Finding and Spatially-Weighted Apertures

3.1 Introduction to monopulse

Monopulse is a technique for determining the angular direction of radiation. It is a highly developed technique in radar, having been developed in the 1940s and still used today in radar [25], sonar, and other applications. The term *monopulse* refers to the capability of the technique to determine the angular location of a target with only one transmitted pulse, which later reflects off the target and is received by the monopulse detector.

As mentioned in Chapter 2, we group the monopulse technique into the beamformers of Brandstein's framework. However, instead of constraining the sensor's response to a particular angular profile, which is beamforming, monopulse is the simultaneous comparison of the amplitudes or phases of two stationary, different-shaped beams. It has also been shown that using derivative-matched apertures can produce a beam comparison result that is non-dispersive, or frequency independent [14]. The interest in the use of a monopulse device as an acoustic direction-finding technique is motivated both by the applications of such a device and by the simplicity of the

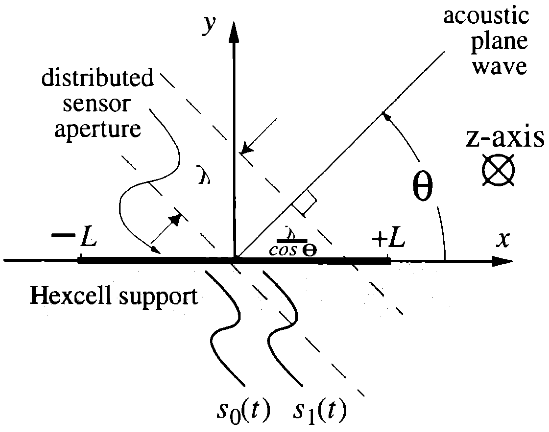

Figure 3-1: Side view of continuous sensor

nondispersive, thus wideband, monopulse technique.

3.2 Signal model

Suppose that two coincident, continuously distributed acoustic-sensing apertures lie on the x-z plane, as shown in Figure 3.2, and that a plane wave of frequency Ω impinges the surface with angle θ from the positive x axis. The pressure wavefront moving across the surface can be expressed as a complex waveform with real amplitude P.

$$p(\mathbf{x}, t) = Pe^{j(\frac{\Omega}{c} cos\theta x + \Omega t)} \tag{3.1}$$

The continuously distributed apertures act as a collection of infinitely small discrete sensors, forming an electrical signal that is the sum of the waveform over the area of the aperture. Because we assume a plane wave, the sum can be expressed as a simple integral in the direction of travel, weighted by the net acoustic response of the aperture, w_i, which depends on the shape of the aperture and on the efficiency of the piezoelectric sensor and can be expressed as a function of x. To simplify the math, we will also assume P is real and lump it into w_i.

$$\begin{aligned} s_i(t) &= \int_{-L}^{L} w_i(x)e^{j(\frac{\Omega}{c}cos\theta x+\Omega t)}dx \quad for \quad i=1,2 && (3.2)\\ w_i(x) &= 0 \quad for \quad |x|>L && (3.3)\end{aligned}$$

Noting that the limits of 3.2 can be extended to ±∞ and substituting the trace wavenumber, $\tilde{k} = -\frac{\Omega}{c}cos\theta$, into 3.2, we can see that s_i equals the product of a time varying exponential and the Fourier transform $W_i(\tilde{k})$ of $w_i(x)$.

$$\begin{aligned} s_i(t) &= [\int_{-\infty}^{\infty} w_i(x)e^{-j\tilde{k}x}dx]e^{j\Omega t} && (3.4)\\ s_i(t) &= W_i(\tilde{k})e^{j\Omega t} && (3.5)\end{aligned}$$

If our aperture weightings w_1 and w_0 can be formed so that $w_1 = \frac{dw_0}{dx}$, then $W_1(\tilde{k}) = j\tilde{k}W_0(\tilde{k})$ by the derivative relation of Fourier transforms. The ratio of signals that are related by this derivative-matching constraint is shown in 3.7, and if s_1 is integrated as in 3.8, the dispersion is eliminated in 3.9.

$$\begin{aligned} \frac{s_1(t)}{s_0(t)} &= \frac{W_1(\tilde{k})e^{j\Omega t}}{W_0(\tilde{k})e^{j\Omega t}} && (3.6)\\ &= j\tilde{k} = -j\frac{\Omega}{c}cos\theta && (3.7)\\ s_1'(t) = \int s_1(t)dt &= \frac{1}{j\Omega}W_1(\tilde{k})e^{j\Omega t} && (3.8)\\ \frac{s_1'(t)}{s_0(t)} &= -\frac{1}{c}cos\theta && (3.9)\end{aligned}$$

The direction cosine, defined in 3.9, is the desired result on the monopulse technique, as it depends only on the angle of incidence and distinguishes waves traveling in the positive x-direction from those in the negative x-direction. To find the direction cosine along the z-axis, another monopulse sensor or set of spatial weightings is required.

3.2.1 Example weightings and weighting transforms

An obvious pair of derivative-matched aperture weightings is the triangular and boxcar weightings as proposed in [13] and shown in Figure 3-2. These weightings will be employed in our prototype, which is described in more detail in Chapter 4. For 3.2, we had lumped the pressure wave's amplitude P and the efficiency of the sensor material into the weighting, and ideally the efficiency would be uniform across the surface, allowing us to vary the weighting simply by changing the physical size of the apertures. The efficiency is not necessarily uniform, but assuming the material is uniformly sensitive and that $P = 1$, the formulas for these weightings are as follows, where *u(x)* is the unit step function, L is the length of the aperture along the x axis and K is the height of the aperture along the z axis:

$$\begin{aligned}
w_0(x) &= \frac{K}{L}(x+L)u(x+L) - 2\frac{K}{L}u(x) + \frac{K}{L}(x-L)u(x-L) && (3.10)\\
W_0(\tilde{k}) &= \frac{K}{L}\left(\frac{e^{j\tilde{k}L}}{(j\tilde{k})^2} - \frac{2}{(j\tilde{k})^2} + \frac{e^{-j\tilde{k}L}}{(j\tilde{k})^2}\right) && (3.11)\\
&= \frac{4K sin^2(\frac{-\Omega cos\theta L}{2c})}{\tilde{k}^2 L} && (3.12)\\
w_1(x) &= Ku(x+L) - 2Ku(x) + Ku(x-L) && (3.13)\\
W_1(\tilde{k}) &= j\tilde{k}W_0(\tilde{k}) && (3.14)\\
&= \frac{(-j\frac{\Omega}{c}cos\theta)4K sin^2(\frac{-\Omega cos\theta L}{2c})}{(-j\frac{\Omega}{c}cos\theta)^2 L} && (3.15)\\
&= \frac{-j4K sin^2(\frac{-\Omega cos\theta L}{2c})}{\frac{\Omega}{c}cos\theta L} && (3.16)
\end{aligned}$$

The magnitudes of the ideal wave transforms are shown in Figure 3-3. As indicated in 3.14 and 3.11, W_1 is purely imaginary (coming from an odd spatial weighting), and W_0 is purely real (coming from an even spatial weighting)[?]. The constants used for these calculations correspond to the prototype sensor we have constructed ($L = 3.86cm, K = 5.1cm$) and the speed of sound, $c = 344m/s$.

The angle, frequency, and length each effect the beam width of the main lobe of the W_0 transform, which has a first zero where $(\frac{-\Omega cos\theta L}{2c}) = \frac{f cos\theta L}{c} = 1$. For

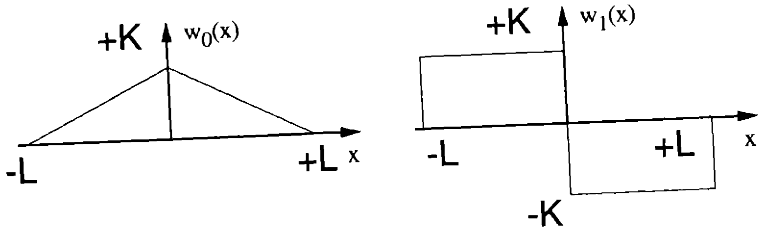

Figure 3-2: Example derivative-matched spatial weighting

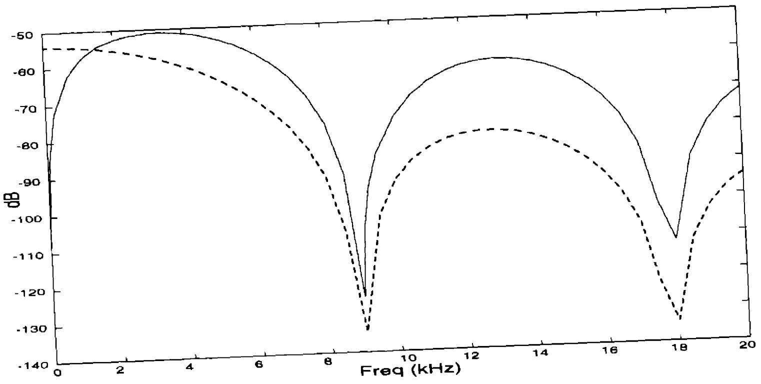

Figure 3-3: W_1 and W_0 transforms at 0 degrees from surface

our chosen dimensions, the beam width is just under 10 kHz and almost 50° from broadside. The beam width is an important factor when weighting errors become a reality (see Equation 3.17 and accompanying discussion). The derivative-matched weightings of a monopulse sensor could be approximated using discrete sensors [15]; however, the bandwidth of discrete element arrays depends on the spacing of the arrays and the error of the discrete approximation causes the output signals to be related by a frequency-dependent factor. Thus, our investigation uses distributed aperture shadings implemented using a piezoelectric sensor.

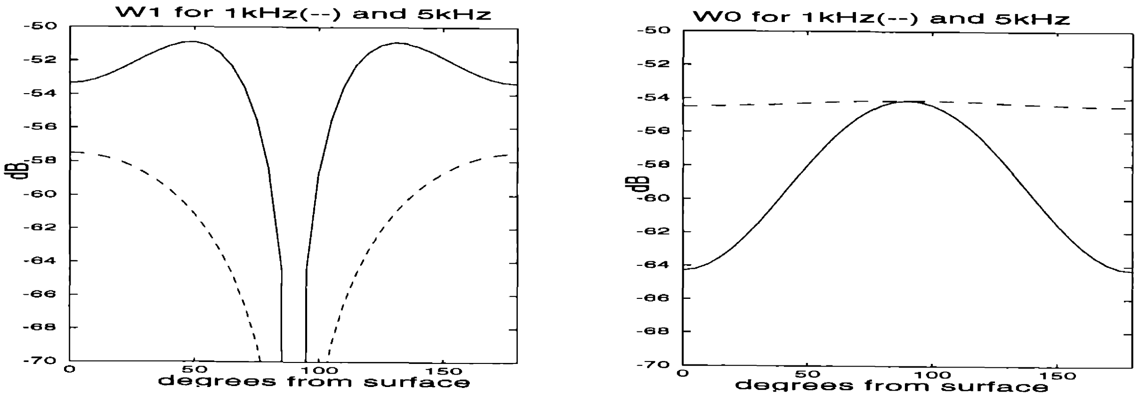

Figure 3-4: W_1 and W_0 transforms' theta responses, 1kHz and 5kHz

3.3 Previous work

The current investigation is a direct extension of the work [10] done at the Charles Stark Draper Laboratory in Cambridge, Massachusetts, by Shawn Burke with the collaboration of Jim Hubbard, Joe Paradiso, and others. This effort was focused on underwater active sonar applications, especially for autonomous underwater vehicles (AUVs) [13]. Below we will present the Draper work in brief and summarize the results of the investigations.

3.3.1 Characterization of piezopolymer acoustic direction finder for underwater sonar

The device characterized by Burke exhibited the weightings just described and was mounted hydrostatically – i.e., the PVDF sensing foil was rigidly bonded to a copper-clad, polyimide substrate and encapsulated beneath a layer of polyurethane to attain a good impedance match to water. Electronics [19] similar to those that will be described in Chapter 4 were used to buffer the sensor's signals.

The characterization of the transducer was performed underwater with gated sinusoids at 24 kHz and 70 kHz [9], [?]. Hilbert transforms were utilized [8] as smoothing functions to decrease the variance of the direction cosine estimates; and for high signal levels, angle resolutions approaching 0.11° (at 24kHz) and 0.075° (at 70 kHz) were obtained within the main lobes of the sensor at the respective frequencies. The stability of the phase measurement extracted from the ratio of numerator and denominator Hilbert transforms provided a metric for bearing quality – i.e., a phase that was neither 180° nor 0° indicated that the signals received were corrupted by reverberation.

Design rules developed at Draper [7] to minimize the effect of shading errors on the monopulse ratio consisted of using the sensor within the main lobe of the denominator signal's beam. Equations 3.17 to 3.20 show how a large response from the denominator signal will decrease the effect of $\Delta(x)$, which adequately describes the error for both shadings.

$$\begin{aligned} w_1(x) &= \frac{d[w_0(x) + \Delta(x)]}{dx} && (3.17) \\ \frac{s_1}{s_0} &= -j\frac{\Omega}{c}cos\theta[1 + \frac{\Delta(\tilde{k})}{W_0(\tilde{k})}] && (3.18) \\ \frac{\mid \Delta(\tilde{k}) \mid}{\mid W_0(\tilde{k}) \mid} &<< 1 && (3.19) \\ [\frac{\Delta(\tilde{k})}{W_0(\tilde{k})}] &\sim 0 && (3.20) \end{aligned}$$

3.3.2 Other applications of spatial weighting

Tapered apertures are commonly used in the amplitude-shading of discrete hydrophones to form beams with reduced sidelobes [5] (e.g., if you spatially weight the transducer amplitudes with an appropriately shaped windowing function, sidelobes can be suppressed). One interest beyond such applications and the monopulse architecture in this work is in extending the use of distributed apertures to embed arbitrary system functions onto the sensing surface of a continuous transducer such as PVDF. Two suggested applications [24] include (1) averaging noise across an aperture much longer than the wavelength of averaged frequencies and (2) forming directionally sensitive weightings for other purposes (e.g., beamsteering). This thesis examines the feasibility of constructing a continuous, tapered-aperture acoustic transducer that operates in air at audio frequencies, and concentrates on the monopulse application. These other possibilities are the subject of ongoing research.

Chapter 4

Construction and Test

4.1 Construction

Here we describe the piezoelectric material used in the sensor fabrication, the design of the sensor for use in air, and the integration of the electronics.

4.1.1 Polyvinylidene fluoride (PVDF)

Polyvinylidene fluoride (PVDF), first developed in the 1960s, is used in a variety of applications ranging from sonar to pressure-sensitive microphones. It is relatively inexpensive and readily available, making it suited for use in ubiquitous direction-finding applications [20]. Our monopulse sensor, shown in Figure 4-1, consists of a 0.28 μm-thick, silver-inked sheet of PVDF.

PVDF is a piezoelectric polymer film that can develop a voltage across its faces in response to an applied normal force. A sheet of PVDF can be thought of as a planar array of voltage impulses, the values of which are proportional to the normal force at each point in the plane. A subset of the array of impulses can be summed by forming charge-collection electrodes on both sides of the PVDF over the desired area. In this way, the shape of the electrode dictates the spatial shading or weighting of the resulting signal.

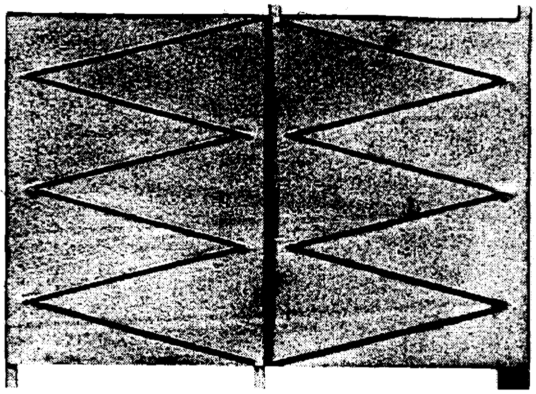

Figure 4-1: New monopulse sensor prototype

4.1.2 Design for use in air

As mentioned in Chapter 3, Draper's monopulse direction-finder prototypes were mounted on a rigid surface and used underwater at ultrasonic frequencies. Our prototype, in contrast, was adapted for use in air at audio frequencies, especially for voice (< 4000 Hz). This adaptation to air and to the audio range required changes in the mounting of the sensor (as hydrostatic mounting is no longer efficient because of impedance mismatch) and in the size of the sensor (from beamwidth considerations).

Mounting

The PVDF foil was mounted with 3M Spray Mount^{TM} artist's adhesive (No. 6065) onto a plastic hexcell support (Part no. PC 125-C-4.0, Plascore, Zeeland, MI; 2.5-3 mm thick and 4 mm in diameter); and the ground plane of the foil was placed outward to act as an electrical shield over the sensing apertures, as shown in Figure 4-2. Hexcell is a lightweight, inexpensive core material consisting of miniature hollow cylinders. It is used in various industrial applications requiring high compression strength, and it is used here because of its rigidity and its ability to match the PVDF sensing surface to the impedance of air. The PVDF stretched across each cell acts as a microphone diaphragm, and the signals from all cells are added according to the

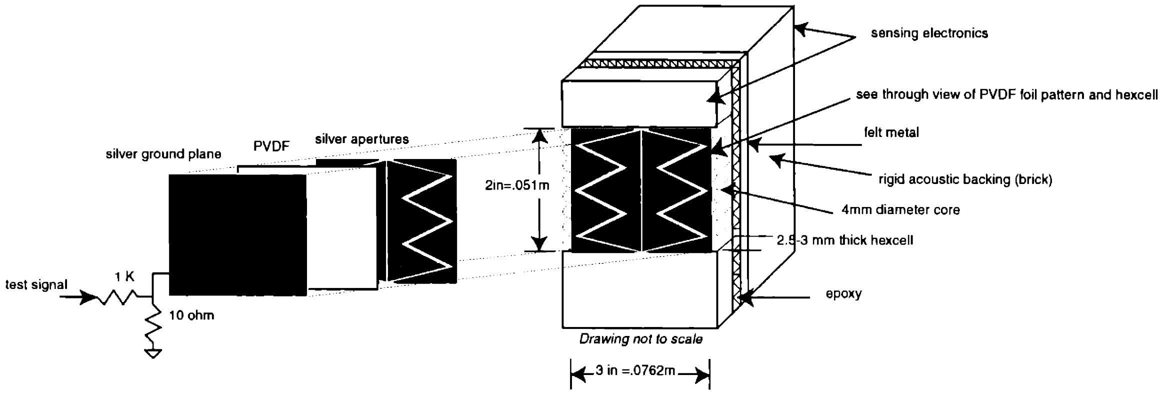

Figure 4-2: Prototype sensor

spatial weighting of the subaperture electrodes, which are silver-inked onto the inner surface of the PVDF (Figure 4-2).

The need for a regular and fine-walled support structure suggested that we first use the available plastic hexcell before experimenting with other materials. Other potential candidates for a mounting substrate include ceramic or glass; these materials are desirable because they are electrically insulating and acoustically rigid. However, we could not find a hexcell structure of ceramic or glass for our tests. Aluminum hexcell suffers from resonances in the audio range and from its electrical conductivity, which would short the subapertures on the bottom of the foil.

The hexcell, or any cell structure, may introduce a number of errors in the spatial weighting. These errors include quantization from the sectioning of foil into discrete circular regions, nonuniform sensitivity within each circular region, cell-to-cell coupling, and irregular tension. A discussion of these errors can be found in Chapter 5.

An essential step in the mounting of the PVDF to the hexcell is the tensioning of the foil. PVDF foil can be characterized by three coefficients which describe the relation between charge produced across the foil and the mechanical stress applied to one of the foil's three orthogonal axes. For our foil, horizontal stress (along the lengthwise dimension of the foil, "3-1" coupling in the piezoelectric nomenclature [20]) produces the maximum output, because as the foil vibrates within a cell, it stretches horizontally against the cell wall, producing a corresponding output voltage. Stress along the vertical (thickness) axis of the foil ("3-3" in the nomenclature) produces significantly smaller outputs [20]. Thus, the foil must be stretched horizontally to produce significant signal. To boost the audio efficiency even more, extra tension could be applied to the foil by creating a vacuum [1] within each individual cylinder of the hexcell material. In the interest of simplicity, this was not done for these experiments.

Prior to the stretching and bonding of the foil to the hexcell, the hexcell was epoxied to a sheet of acoustic felt metal (Brunswick Technetics, DeLand, FL) which itself was epoxied to a brick. The felt metal served as an acoustic absorber and an electric shield; and the brick was chosen as a very stiff backing, a conservative measure for initial tests, ensuring no coupling from the sensor's support structure. A much more attractive and useful option could be a solid, smaller block of ceramic. It was determined that the felt metal was unnecessary as a sound absorber, and copper mesh was used behind the sensor as an electric shield in a second prototype.

Connecting the foil to sensing electronics proved to be a delicate process. An initial prototype used copper tape to adhere to the silver leads of the foil; the copper tape was then bonded to the electronics with silver epoxy (Circuitworks^{TM} CW2400 from Chemtronics, Inc., Kennesaw, GA). Unfortunately, this prototype failed continuously because it lacked a reliable electrical connection. It was much more reliable to solder a stranded wire jumper to a pad of brass shim stock and then to epoxy the foil's silver leads to the brass pad, as originally detailed by Burke and Sullivan [6],[27]. It is important to note that the epoxy had to be cured near room temperature, as significantly heating the PVDF depolarizes it – destroying its ability to work as a sensor. An earlier example setup of the hexcell mounting is shown in Figure 4-3.

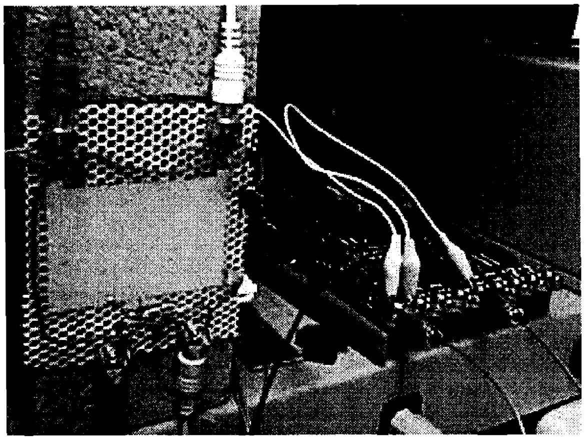

Figure 4-3: Test setup

Size

There are several competing considerations relating to the size of our sensor: signal levels, beamwidth, and shading errors. First, a large sensor increases the total voltage output and thus improves signal quality. However, a small sensor is less directive and can be used efficiently over a larger angular range. Finally, larger staves are affected less by hexcell quantization, as many cells are combined together per subaperture. Because the achievable signal levels and the effect of the hexcell upon shading was not fully understood at the beginning of this thesis, we chose the dimensions based on beamwidth considerations.

The electrodes covered a 2 in (5.1 cm) x 3in(7.62 cm) area of the PVDF, making it the width equal to one wavelength of $\frac{c}{\lambda} = \frac{344m/s}{.0762m} = 4414$Hz. With increasing angle from the surface, the nulls of the incoming waveform are stretched farther apart (??). At 90° (broadside), the waveform impinges the entire surface simultaneously. For an angle range of ±60° from broadside, the wavelength of the frequency that wraps on the foil is $\lambda = (7.62m)cos30^\circ = 6.6cm$, which corresponds to a frequency of 5145 Hz. Most of the frequency content in voice lies below these cutoffs, so it is hoped that the sensor will perform well in the voice band under the current design.

The prototype foil replicates a triangular pattern [?] three times along the vertical axis in order to minimize height-dependent effects on the beamwidth[?], but the number of apertures is still only four, as the vertical subapertures are connected across the foil by conductive bridges.

4.1.3 Electronics

As the front-end electronics were mounted right at the foil electrodes, they were kept as simple as possible. The signal conditioning electronics consisted only of a JFET voltage follower (see Figure 4-4), placed on mini-circuitboards, that drove a short length of cable to the main signal conditioning card, located on the back of the brick (Figures 4-5 and 4-2). There it was capacitively coupled to two operational amplifier (gain = 33.2) stages for each of the four subaperture channels(see Figure A). To match the aperture signals as closely as possible, the gains were set with 1% resistors. The channels were then bused via coaxial cables of type RG-58U approximately 10 feet to the data acquisition system, a four-channel, simultaneously-sampled National Instruments 6110E data acquisition board (Figure 4-5).

To quickly and easily check that the sensor was operating as expected, an integrated (low-pass filtered) numerator signal s_1 and a denominator signal s_0 (4-5) were formed using op amps and could be probed with an oscilloscope during test. Also, to verify the operation of each of the channels, the ground plane was floated slightly above ground with a 10 Ω resistor (see Figure 4-2). This allowed a test signal to be injected through the ground plane into all the channels. The amplitudes of each subaperture were verified to be within a few percent of one another before proceeding to acoustic tests.

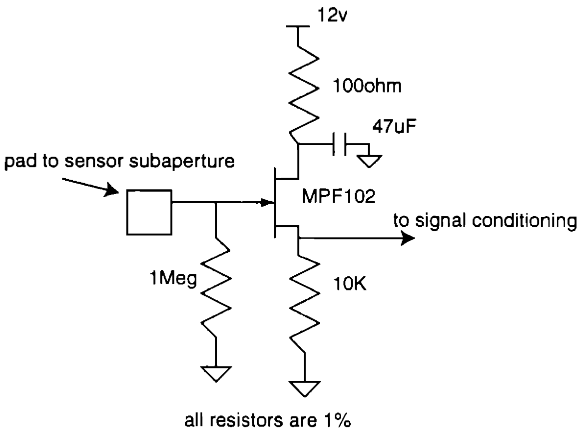

Figure 4-4: Schematic of sensing JFET voltage follower

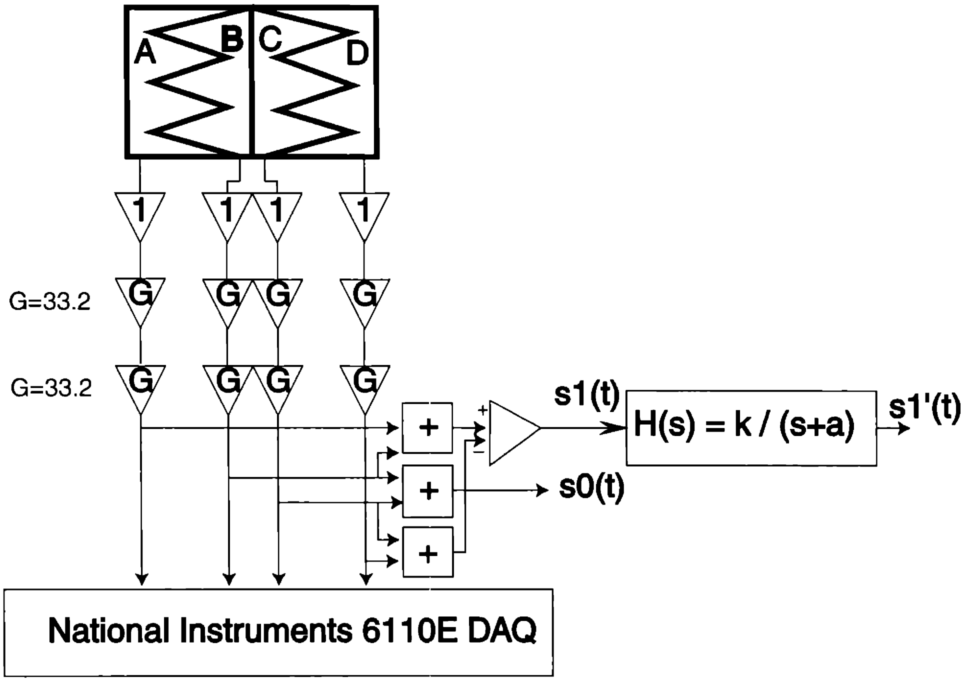

Figure 4-5: Schematic of summed signals

4.2 Test

4.2.1 Test setup

The tests were performed in a laboratory 2.62 m (8.6 ft) high, 3.65 m (12 ft) wide, and 7.11 m (23.3 ft) long. The floor consisted of aluminum removable tiles covered with industrial carpeting, the ceiling consisted of hanging foam tiles, and the walls were painted drywall. The two end walls were covered by white boards from top to bottom, and one wall to the right and behind the test setup was glass. Lab desks were located against the walls along the path from speaker to microphone, and metal shelves were placed on top of these tables. Noise sources included a computer fan and a digital oscilloscope cooling fan. These noise sources were located behind the source, as was the observer during the tests. Although this environment was fairly noisy and reverberent, it served as a real-world test environment. Also, the data analysis extracted first arrival data, avoiding corruption by reverberation.

As shown in Figure 4-6, a Bruel&Kjær source (Model 4219), driven with a Hafler P1500 amplifier, was placed 1.22 m high on a speaker stand and 2 m from the monopulse sensor, which was also placed on a speaker stand 1.22 m high and within a flat baffle of foamcore panel measuring 1.5 m wide and 1 m tall. A calibrated microphone (B&K condenser microphone of type 4138) was also placed within the baffle, approximately 10 cm above the center of the sensor. This setup provided a time of arrival as follows: (direct path) $\frac{2m}{344m/s} = .0058sec$, (first reflection) $\frac{3.155m}{344m/s} = .0092sec$, (reverberation-free interval) $.0092 - .0058 = .0034sec$.

The sensor was placed at a distance of 2 m from the source to put it in the far field and to ensure that the received signals were plane waves. The far field criterion [2] is that the sound pressure decreases linearly with radial distance r from source to receiver. To be met, the transmitting array must be small compared to r, and r^2 must be large with respect to $\frac{\lambda^2}{36}$, which is satisfied here even for our lowest test frequency of 500 Hz.

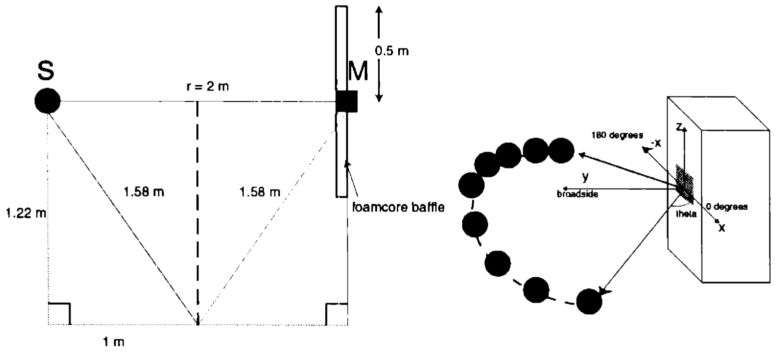

Figure 4-6: Test setup

The source can be modeled as a rigid circular piston in the end of a long tube, since the back and sides of the speaker are shielded. The source is unidirectional at 500 Hz, and slightly focused with one forward-pointing beam with beamwidth of approximately 120°[2]. The lack of sidelobes helped suppress the corruption of data due to reverberation.

The source was moved through an angular range of ±40° in approximately 10° increments from broadside (50° – 130° from positive x-axis). Although more prompt reflections coming off the desk shelves may be present for the tests at higher angles, our data looked relatively clean.

Additionally, the baffle was removed and data taken over several frequencies to determine the effect of diffraction on the monopulse ratio. Diffractive effects [26] can be significant if the wavelength of excitation drops below the size of the sensor surface, which was effectively extended by the baffle.

In one application, the monopulse sensor could be used to track a moving person or to switch among several speakers in the same room. Several tests were performed using voice and other cues to determine the sensor's performance with less controlled inputs. The sensor was placed in the baffle for these tests.

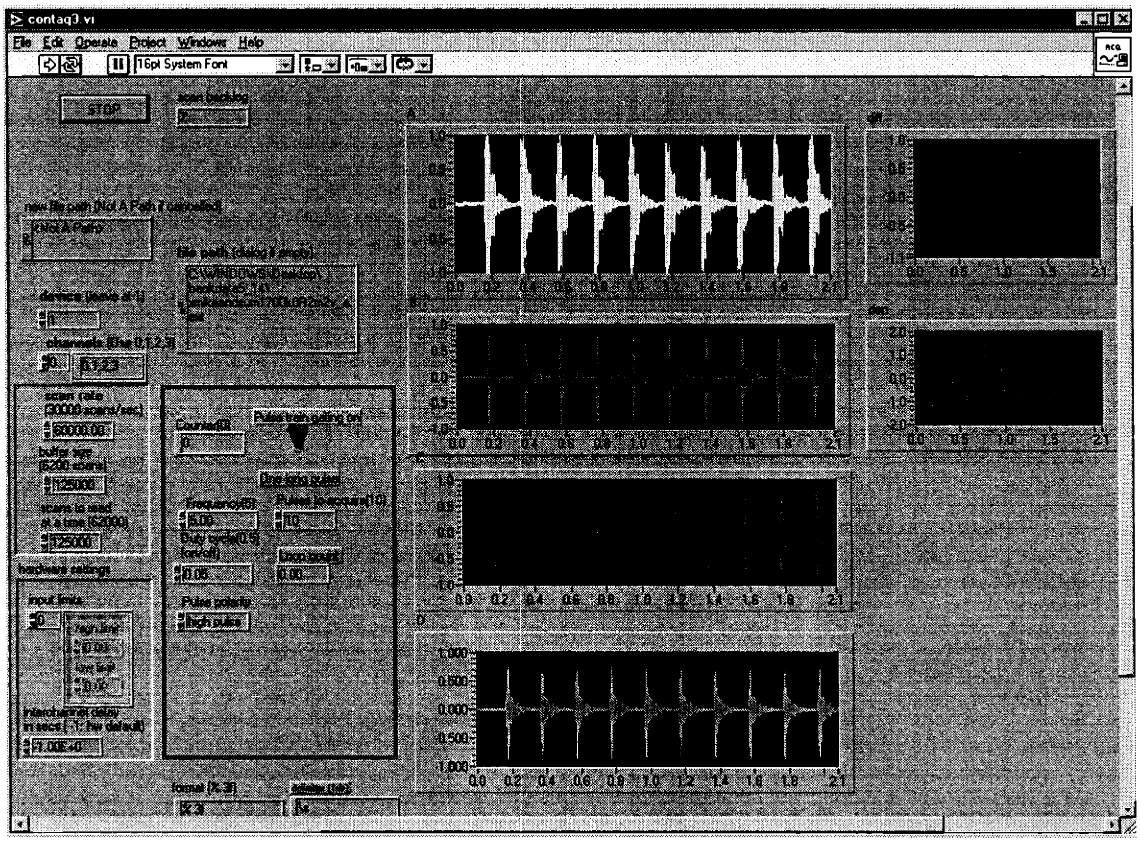

channels: 0,1,2,3

scan rate: 60000.00

buffer size: 125000

scans to read at a time: 125000

interchannel delay in secs: 1.00E+0

Counter: 0

Frequency: 5.00

Pulses to acquire: 10

Duty cycle (on/off): 0.05

Loop count: 0.00

Pulse polarity: high pulse

format: %.3f

Figure 4-7: Labview data acquisition display

4.2.2 Data acquisition

Several virtual instruments (VI's) were developed to control data acquisition (see Figures 4-7 and 4-8). The VI shown acquired data at 60,000 samples/s and provided a two-second, 5 Hz, 5% duty cycle waveform (or ten gates of 20 ms duration within 2 seconds) to activate a Hewlett Packard 12332 waveform generator, which drove the source through the Hafler amplifier. The plots above show the data acquired from the four subapertures ($A - D$) and from the difference and sum signals (diff,den). Data was acquired and saved for processing offline using Matlab.

The VI shown in 4-8 was used to demonstrate the operation of the monopulse sensor in real-time and utilized much of the same processing as will be discussed in

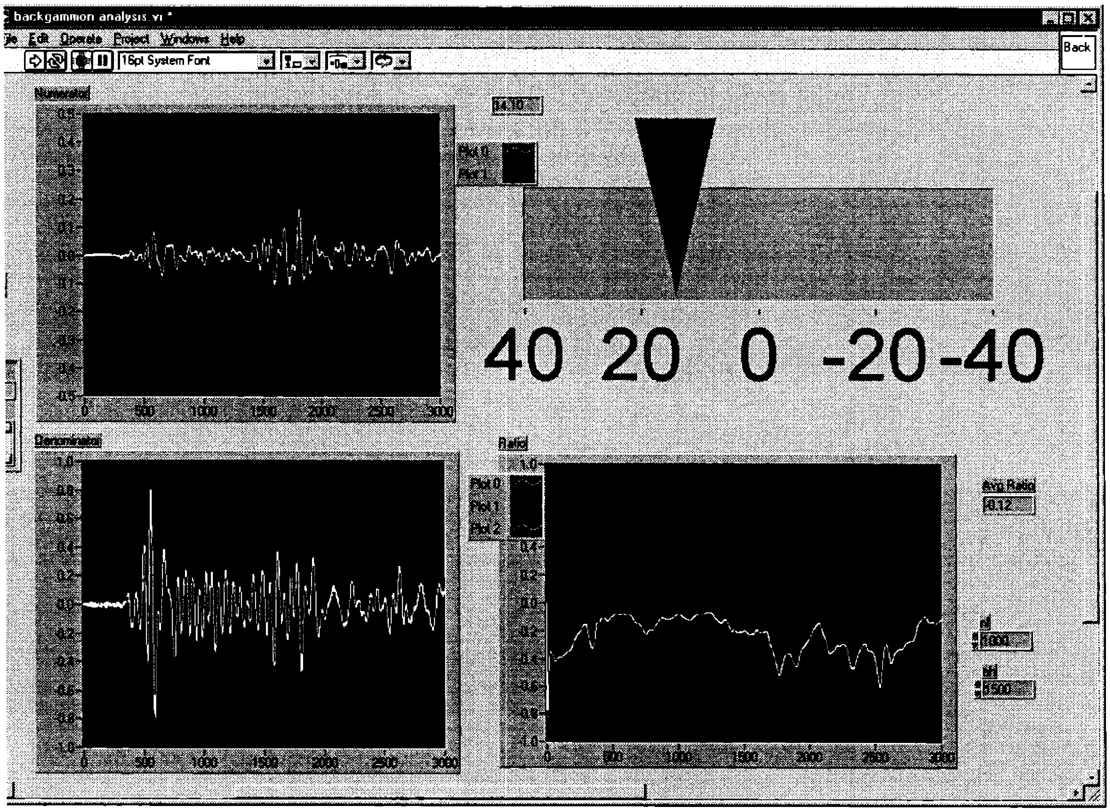

Figure 4-8: Labview real-time direction finder

Chapter 5. The numerator and denominator signals of a finger snap are superimposed over their envelopes, and the ratio signal is the ratio of envelopes. The ratio is relatively flat before the first reflection at sample 1500, indicating that this period of time could be used to extract an angle estimate. Such an estimate is found (and shown with the needle) by averaging the ratio during this valid period.

Chapter 5

Simulations and Data Analysis

In this chapter we present the predictions of simulations, the experimental data, and the interpretation and comparison of the two data sets.

5.1 Simulations

Simulations were coded in Matlab to model the effects of the actual, non-ideal weighting realized in the stave that we built. The signals generated by the simulation for the actual weightings were fed into the same Matlab code used to process the real data, and similar graphs were generated. We will discuss the models for ideal and non-ideal weighting and then show the results of the simulations. In addition, we generated the monopulse ratios for a sensor with unmatched apertures, as described in Chapter 3, for comparison with acquired data.

5.1.1 Ideal and non-ideal weighting models

The models constructed included an ideal weighting model, a non-ideal weighting model with fine resolution, and a non-ideal weighting model with course resolution (as an approximation to the effects of the hexcell mounting). We will refer to the math in Chapter 2 and the Matlab code in Appendix B in describing each of these models in more detail and in discussing the results of the simulations. Although one could calculate the error transforms $\Delta(x)$ as described in Chapter 2, we allow the simulations to carry the error into the time domain signals and the ratio, which are more intuitively evaluated.

Ideal model

The ideal weightings are a triangular weighting (w_0) and a boxcar weighting (w_1). The slope of the triangular weighting, for an ideal sensor, is equal to the ratio of the sensor's length along the positive (or negative) x-axis to the sensor's length along the z-axis. Equation 3.10 shows $\frac{K}{L} = \frac{5.1cm}{3.86cm}$. Similarly, the amplitude of the boxcar weighting is proportional to its physical length along the z-axis, 5.1 cm. These weightings are discretized to one pixel's resolution, which is based on the bitmap of the actual foil and the dimensions of the foil. The horizontal step size, Δx, is equal to $\frac{3.86cm}{325pixels}$, or .119 mm; the vertical step size, Δz, is $\frac{5.1cm}{433pixels}$, or .118 mm. Thus, weighting functions $w_{1,2}(x_i)$ are equal to the product of the vertical step size and the number of charge-collecting pixels in the z direction at x_i (Equation 5.1).

The signals resulting from these weightings were approximated as shown in Equation 5.2. The discrete-time exponential was generated with the same sampling period that was used in data acquisition. The appropriate real or imaginary parts of the signal were then selected. The dashed line in Figure 3-2 shows the ideal shading of our sensor.

$$
\begin{aligned}
w_{1,2}(x_i) &= (pixels_i)_{1,2}\Delta z && (5.1)\\
s_i(t) = W_i(\tilde{k})e^{j\Omega t} &\cong W_{di}(\tilde{k})e^{j\Omega n T_s} && (5.2)\\
W_0(\tilde{k}) = \int_{-L}^{L} w_0(x)e^{j\frac{w}{c}xcos\theta}dx &\cong \sum_{i=-n}^{n} \Delta x w_0(x_i)e^{j\frac{w}{c}x_i cos\theta} && (5.3)\\
W_1(\tilde{k}) = \int_{-L}^{L} w_1(x)e^{j\frac{w}{c}xcos\theta}dx &\cong \sum_{i=-n}^{n} \Delta x w_1(x_i)e^{j\frac{w}{c}x_i cos\theta} && (5.4)\\
x_i &= i\Delta x && (5.5)
\end{aligned}
$$

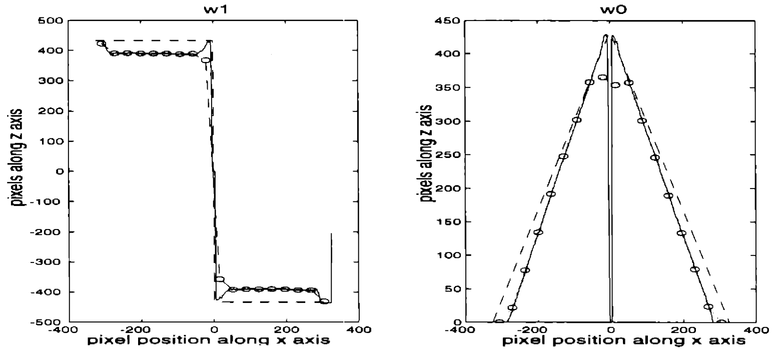

Figure 5-1: Ideal and non-ideal weightings for W_1 and W_0

Non-ideal models

The non-ideal weightings assumed that inter-cell coupling did not occur and were formed by scanning the actual foil on a flatbed scanner, loading the bitmap into Matlab, and scaling the dimensions of the bitmap to match that of the foil. The weightings from the bitmap are shown in Figure 5-1, overlaid with the ideal shadings (dashed lines). The non-ideal weighting with course resolution (see circled points of Figure 5-1), accounting for the hexcell's discretization of the foil into small diaphragms, was computed by using a step size of 4.2 mm (the diameter of the hexcell cylinders plus cell-wall thickness and inter-cell spacing) in the discrete integral approximation of the weighting transform. The weighting used for each step was the average of the pixel weightings across the step.

This is a rough first approximation for the hexcell-induced weighting. A more accurate model might use the original step sizes with a secondary weighting function, which would decrease the contribution from signals close to the cell walls (i.e., close to the 4.2-mm step edges). Thus, the center of each cell would be the most heavily weighted point within its cell.

Untapered monopulse simulation

The sensor is easily adapted to be a regular, untapered monopulse sensor, in which equal-area, adjacent rectangular apertures are used to form a difference signal (numerator) and a sum signal (denominator). The untapered shadings result in a monopulse sensor that is not dispersion-free. To determine the necessity of derivative-matching for dispersion-free monopulse operation over our desired range of frequencies, the ideal ratio for untapered apertures was calculated and compared to acquired data. The data acquired from the untapered aperture was processed similarly as the tapered data, and the results are shown in the section comparing simulations and experimental data.

5.1.2 Simulation results

The normalized ratio of signals generated with ideal shadings was dispersion-free and nearly identical to $cos\theta$, assuring us that the discretized integration in our simulation was a good approximation to a continuous integration for the frequencies of interest. Determining the quality of the non-ideal model's simulation for predicting the sensor's behavior requires the comparison to acquired data; therefore, this discussion is handled in the comparison section.

The non-ideal simulation was also used to determine heuristicly the effect of different settings for envelope and capacitor cutoffs. Ideally, the integration cutoff would be chosen one order of magnitude less than the frequencies of interest, so that the low-pass filter operated like a pure integrator. However, choosing a higher cutoff is beneficial for attenuating 60 Hz noise. Simulations showed that the integrator changed the normalizing slope, but did not change the variance for sinusoidal inputs. Thus, an integrator cutoff of 500 Hz was chosen for the comparisons.

The effect of decreasing the cutoff for the envelope detector's low-pass filter, described in detail by Henderson [15], is to reduce the variance of the ratio by reducing the ripple in the envelopes and eliminating zeros in the envelope of the denominator. A cutoff approximately twice the lowest frequency of interest, chosen because the full-wave rectification effectively doubles the frequency, is a reasonable choice. Simulations did not show significant differences in normalized ratios variance due to lowering the cutoff. We used 1500 Hz as a cutoff for data comparisons.

Zero-mean, pseudo-random noise, uniformly distributed across ± 20mV, was not a good model for the noise. A more accurate model would include a low-level 60 Hz signal, which would result in a DC offset in the ratio. This offset could be subtracted by averaging the signal during low signal levels for at least one 60 Hz period.

Despite the rough models, offset in the ratio was negligible, indicating that the shading mismatches for the numerator signal were not significant.

5.2 Experimental data

5.2.1 Acoustic frequency response and sensitivity

As explained in the construction of the sensor, the outer electrode of the foil was connected to ground by 10 ohms to enable the coupling of an electrical signal into the four sensing electrodes for testing purposes. For example, the frequency response of the conditioning electronics was measured for each subaperture to have a cutoff at approximately 30 kHz, well above the acoustic response's cutoff. By applying a low level test signal separately to each subaperture, we also demonstrated the lack of significant crosstalk between channels.

The acoustic sensitivity of our sensor in decibels, *re* 20 μPa, shown in Figure 5-2, was measured with a Hewlett Packard 3560A dynamic signal analyzer. With ungated noise being output from a Mackie HR824 studio monitor speaker, the HP analyzer performed a real-time FFT of the sensor's sum signal, compensating for the sound pressure levels at the sensor by using input from a calibrated microphone. The gain of the electronics was divided (i.e., 60.8 dB was subtracted from the response data)

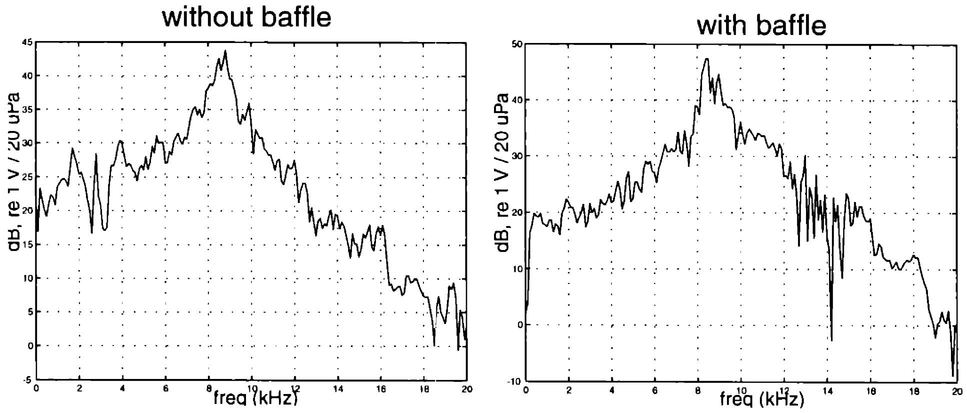

Figure 5-2: Sensitivity in dB, re $\frac{1V}{20\mu Pascal}$, without baffle

to show the sensitivity of the stave.

$$Sensitivity = 20log_{10}\frac{V_{sensor}}{GV_{calib}} \tag{5.6}$$

The spectral instability between 2 and 4 kHz could indicate that a baffle structure is needed to eliminate diffraction effects. This frequency range is important because it is the main portion of the voice band. Also, the response of this device is enhanced around 8 kHz, possibly from an effect of the mounting scheme.

5.2.2 Data manipulation and analysis

Data smoothing

The theory of the monopulse operation suggests that a point-by-point ratio of time waveforms could accurately track the bearing of an acoustic source; in a real-world setting, this is not the case. Noise degrades the signals and their ratio, and when the denominator signal nears a zero-crossing point, the ratio diverges, as shown in Figure 5-3. One way to address this problem is simply taking the ratio during times in which the denominator signal is outside a specified region near zero. However, this method only addresses the zero-crossing problem and does not reduce errors due to noise. Thus, some form of smoothing or averaging of time waveforms is desirable.

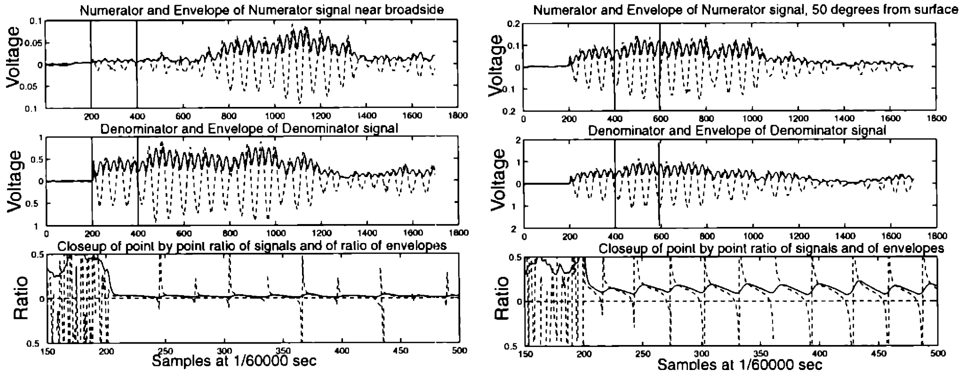

Figure 5-3: Plot of ratios of signals and envelopes for a 1 kHz pulse

There are several different smoothing techniques that suggest themselves: (1) the Hilbert transform method, (2) squaring and smoothing, and (3) rectification and smoothing. The Hilbert transform method, which involves the formation of an analytical signal by the addition of the signal and the signal phase-shifted by 90°, was used at Draper ??. Squaring and smoothing is simpler than the Hilbert transform method and has been used and analyzed extensively [15]. The rectification and smoothing method is perhaps the simplest operation and has been used in spatial hearing research [17] on bandpass signals to detect the onset times of voice and other cues. For the sake of simplicity (it can be implemented with simple discrete components) and despite its non-linearity, we have chosen a full-wave rectification and smoothing algorithm.

The smoothing algorithm was implemented in Matlab with a single-pole low-pass filtering of the rectified waveforms. The numerator and its envelope and the denominator and its envelope are shown in 5-3 for a 1 kHz pulse arriving at the sensor. Note that the numerator displays the nulling action that occurs at broadside (due to the cancellation of the waveform that arrives at all four apertures simultaneously). The nulling action is used to verify correct operation of the sensor before acquiring data.

Triggering

To restrict the formation of a direction estimate to data within the reverberation-free period of a waveform, only the first 3 ms were included after a triggering point set by a simple threshold detector. Because reverberation was often of larger amplitude than the first arrival, a second window was required to prevent reverberation from triggering an angle estimate after the 3-ms window. Equation 5.7 shows how the direction cosine was estimated, as a mean of the sample-by-sample envelope ratios. Here, $s_1'(t)$ represents the integrated difference (numerator) signal.

$$\alpha cos\theta = \frac{1}{N}\sum_{i=1}^{N} sgn(s_1' s_0)\frac{s'_{1,envelope}}{s_{0,envelope}} \tag{5.7}$$

$$N = \frac{3ms}{60,000samples/sec} = 200samples \tag{5.8}$$

Offset errors

There are two sources of an offset error for the direction cosine: rectification and imbalances in shading. Due to the rectification of inputs, even low levels of noise from the sensor or background will be converted into a small DC offset and will be included in the ratio. To properly baseline the envelopes before the ratio is taken, an average of the envelopes could be taken at ambient noise levels and subtracted from the corresponding envelope. However, this approach does not promise to accurately account for the offset present during the 3-ms ratio estimate. For instance, a 20 $\mathrm{mV}_{PP}60Hzsignal'saverageoveroneperiodis$

Offset of about .10 mv for adjusted data to slope, across frequency. Less noise at lower integration cutoff frequencies, but the same noize envelope detectors at various frequencies . also determine ratio condition for untapered apertures (include in section on that)

Finding the DC offset is important for accurate real-time operation; . We chose to use the average of the envelopes for a 3-ms period preceding the pulse as the offset, but the duration of the averaging period could vary with noise levels and input type.

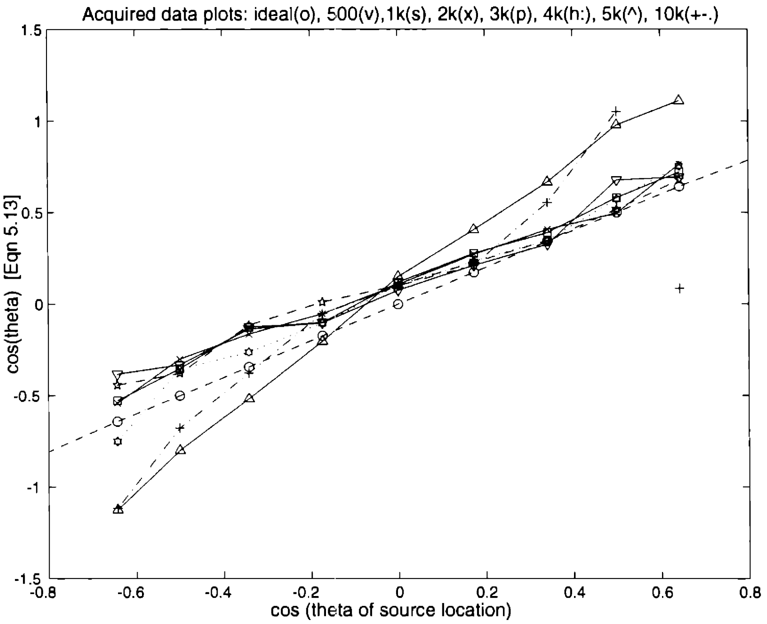

Figure 5-4: Ratios for experimental data

For our tests, the signals were known beforehand.

5.2.3 Monopulse ratios

Gated sinusoids

As discussed in Chapter 4, the source was moved through an angular range of −40° to +40° from broadside (or 130° to 50° from the surface), and ten pulses of a gated sinusoid were acquired to form an angle estimate for each location. The normalized angle estimates for each frequency are shown in Figure 5-6.

The vertical axis in the plots refers to the calculated direction cosine of the data. The horizontal axis refers to the direction cosine of the location of the source. The dashed line indicates the ideal normalized direction cosine, cos θ. The dotted line is the result of the simulated data, and the solid line is the acquired data's angle estimate. The simulation and acquired data required different normalizing gains because the sensitivity of the foil was unknown and therefore could not be preset in

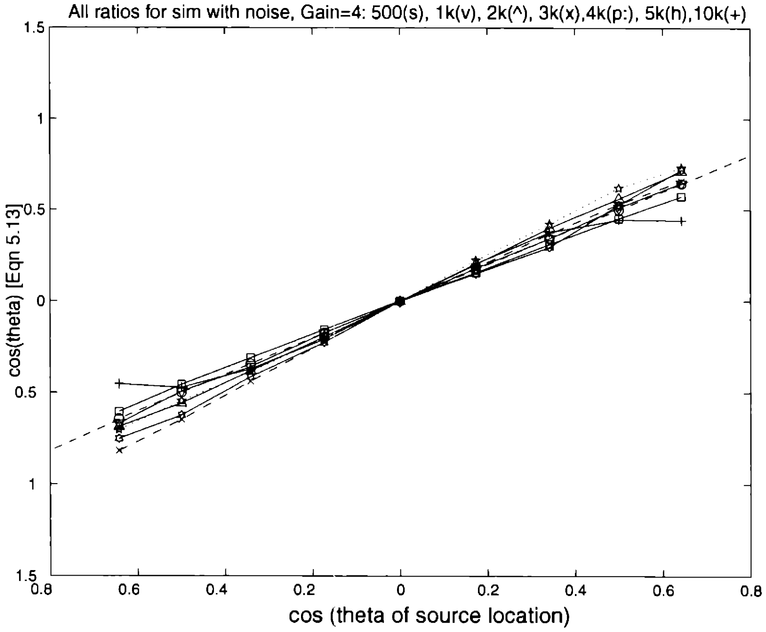

Figure 5-5: Ratios for simulated data

the simulation. The normalizing gains are kept the same for all frequencies to show the dispersion at higher frequencies.

As the simulations predicted, varying the cutoff and integration cutoffs had little effect on the spread of the direction cosine. Thus, a cutoff of approximately 500 Hz for integration and a cutoff of 1300 Hz for the envelope detector were used.

Data variance

A best linear fit, in the least-squares sense, for the data was computed using Matlab's *polyfit* routine, and the resulting normalized slopes and offsets are shown in Figure 5-7. The slopes indicate the amount of dispersion, and the offsets indicate what level of offset is necessary to correct for the noise level and subaperture acoustic mismatch that form residuals in the broadside null.

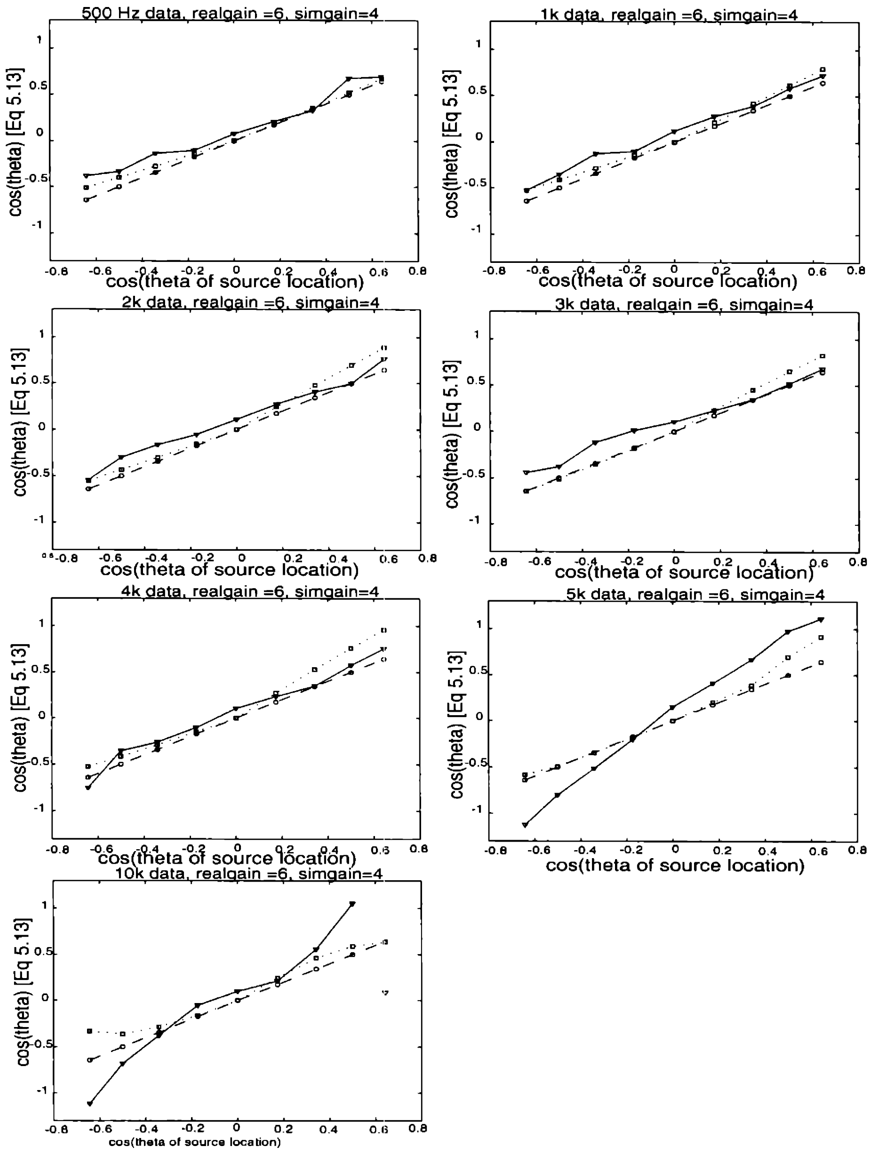

Figure 5-6: Frequency ratio plots

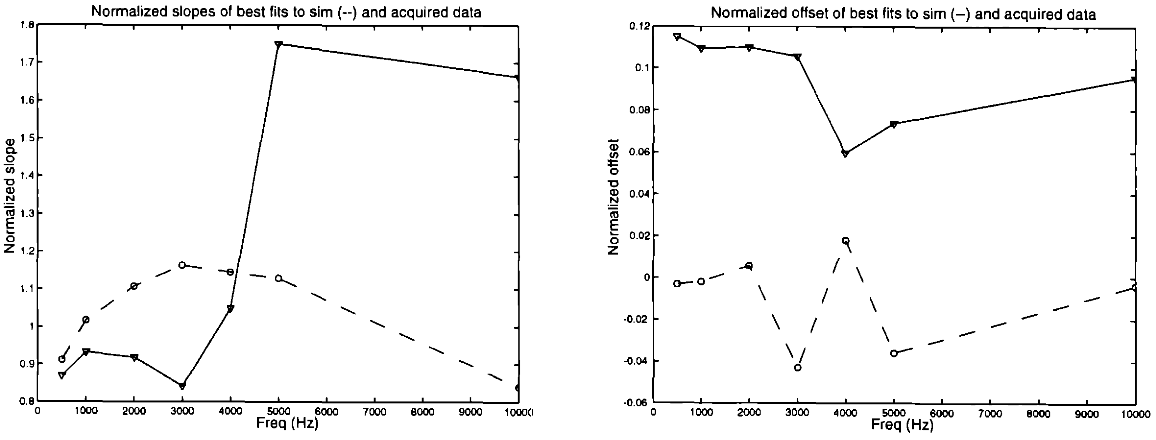

Figure 5-7: Fit slopes and offsets

The variance, σ^2, of the best fit was calculated as shown in 5.9 from [3].

$$\sigma^2 \simeq s^2 = \frac{1}{N-2}\Sigma_{i=1}^{N}(y_i - \beta - \alpha x_i)^2 \tag{5.9}$$

Here, N is the number of points in the data set, y_i are the data points corresponding to x_i, and α and β are the offset and slope of the fit, respectively. The normalized variances for our data and simulations are shown in 5.2.3. The spurious data point in the 10 kHz data at 40 degrees from broadside is omitted from the fitting, yet the variance still increases with frequency. This could be related to the fact that the envelope detector more severely attenuates the 10 kHz waveform, thus reducing the amount of information or the closeness of tracking. Also, there is a zero in the sum beam's frequency response near 10 kHz.

The simulation's best-fit slopes shows that it is nearly dispersion free because the slope is close to flat across frequency.

Voice data

Vocal and other cues were used to test the qualitative performance of the baffled sensor with real-world inputs. The cues used were produced by a single male experimenter and included the following: a hand clap, a finger snap, the word "pay," and the word

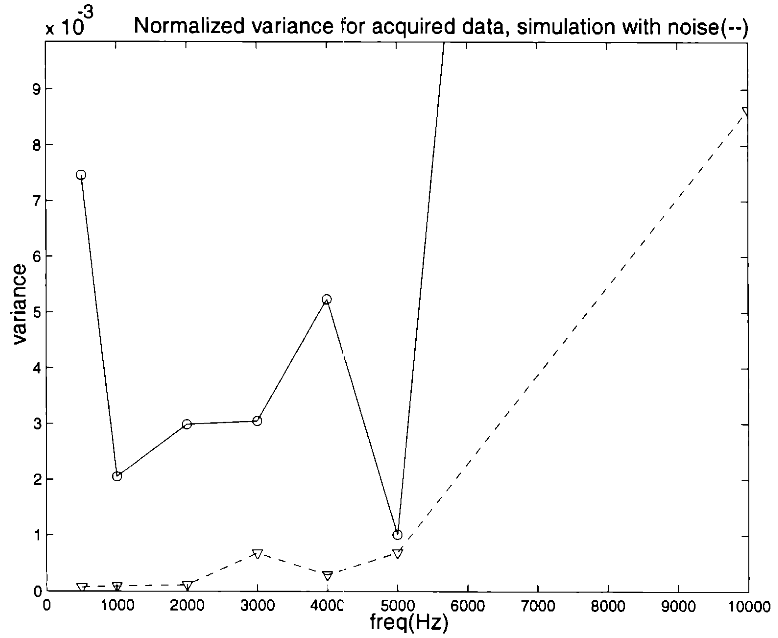

Figure 5-8: Variance for best fits to ratio with frequency

"two." Hand claps provided a high-amplitude impulse source, and the finger snaps provided a smaller amplitude impulse. The "pay" cue, chosen for its abrupt, burst-like transition from stop phoneme to vowel, was shouted in an attempt to produce signals that would not only exceed the sensor's 20 mV peak-to-peak noise level but also rise above the noise quickly enough to allow triggering before the first reflection. The "two" cue was also chosen for its abrupt nature; however, it was spoken above normal speaking level but was not shouted. Other polysyllabic words were used briefly; however, because the signal levels of these more complex sounds were so low, analysis was restricted to the current sounds.

All cues were executed at intervals of approximately 20 degrees and at a distance of 2 m from the sensor. The height of the experimenter was 180 cm, only 22 cm from the center of the sensor. A more rigorous testing would include the use of recordings of various cues placed at smaller and more accurate angle intervals, but these were qualitative tests.

The acquired data was processed with the same integration and envelope detection algorithms as the sinusoidal inputs. The threshold was set to .04 V to trigger on almost any excitation above the noise, and a window of approximately 300 ms was activated upon triggering to prevent another trigger from occuring until after the window. The results are shown in Figure 5.2.3 and the cues' waveforms are shown in Figure 5.2.3. The time and voltage scales are the same for each plot, showing the relative amplitude of the different cues. The dotted lines indicate an uncertainty range of 5° (or $\cos(5°)$) for the angular location of the source, the moving experimenter.

The threshold of 0.04 V works well for the non-voice cues because they rise abruptly and high above the noise level, allowing a good ratio calculation to be completed before the reflections, which can be seen in the non-voice waveforms as a decaying series of spikes. On the other hand, the voice cues will likely not trigger until reverberation has set in, leading to "confusion", in which the angle estimate is an average of the direction of first arrival and of other arrivals.

One strategy to improve the performance for voice cues without degrading the non-voice cues' performance would be to increase slightly the threshold of triggering an angle estimate. This strategy did improve the tracking (not shown) of the "pay" cue, probably because the vowel following /p/ grew very large in amplitude relatively quickly, allowing the angle estimate to be dominated by the first arrival. However, the "two" cue did not improve, likely because of the slower rise and lower amplitude levels.

Another strategy which improved the data for "pay" was lowering the envelope detector's cutoff to approximately 450 Hz, effectively smoothing out the envelope even more and triggering on the vowels in voice, which are lower frequency and tend to have greater amplitude than consonants. However, assuming or favoring certain frequency bands *a priori* defeats the purpose of a broadband monopulse sensor.

Due to its poor sensitivity – i.e., the low response for normal speaking levels – the current monopulse sensor has limited value for tracking a speaker in a room.

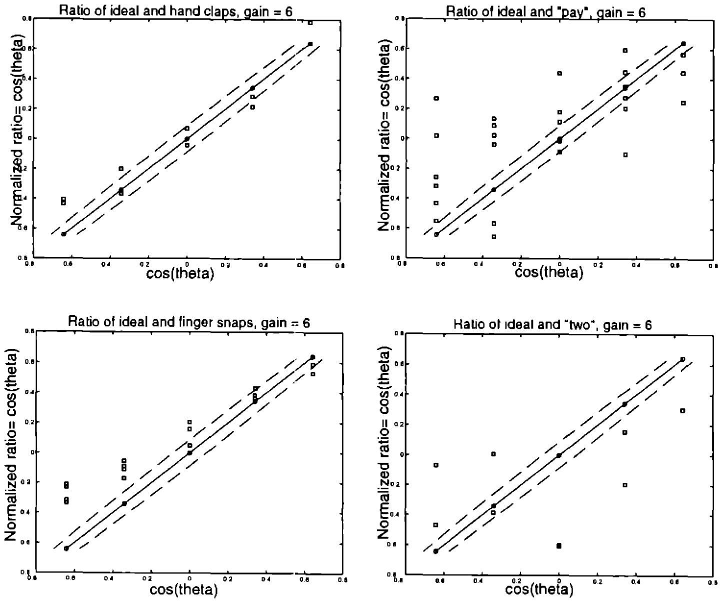

Figure 5-9: Ratios with various samples, threshold set for first arrival

Adding more substantial signal processing to the sensor is not a valid solution because conventional microphone arrays already perform well with such resources. Thus, the real answer lies in increasing the efficiency of the sensor or using cues that are abrupt and high amplitude.

Even if the sensor were adequately responsive to voice cues, to develop a system which can in real-time locate a source also requires an adaptive window. For data analysis, our window of valid data was changed to fit the known data type and the known reverberation time. The method of controlling such an adaptive window is not readily apparent, unless the user is constrained to interact in a certain way.

Unbaffled sensor

The foamcore baffle, shown in Figure 4-6, was used to reduce the effects of diffraction fields [26] at lower frequencies. Previously, tests performed without the baffle indicated that a broadside null was not occuring for the sensor for low frequencies (~1

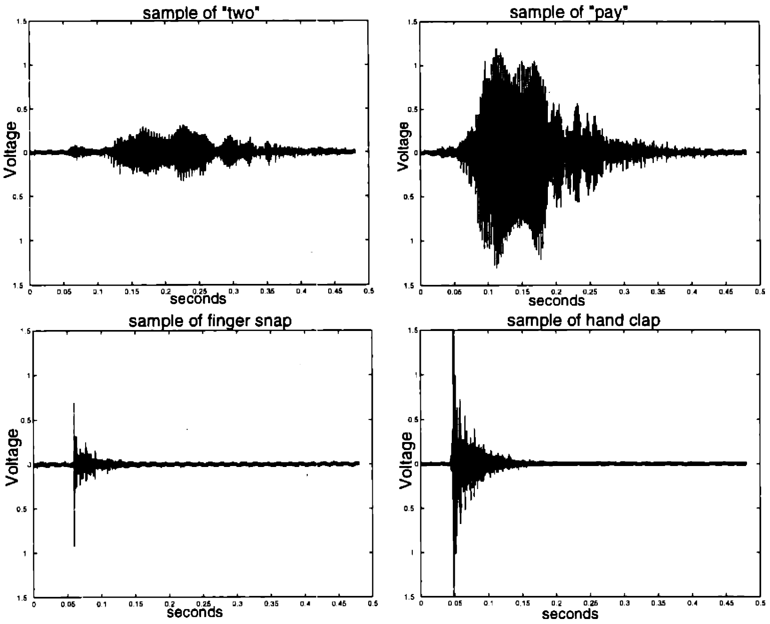

Figure 5-10: Waveforms of voice and non-voice cues

kHz) while at high frequencies the null existed.

Monopulse operation with untapered apertures

The difference or numerator signal of the untapered monopulse sensor is the same s_1 signal as in the tapered sensor. The denominator or sum signal, however, is the rectangular aperture consisting of all four subapertures. The transform of this new weighting and the resulting monopulse ratio are as follows:

$$w_2(t) = Ku(x+L) - Ku(x-L) \tag{5.10}$$

$$W_2(\tilde{k}) = K[\frac{e^{j\tilde{k}L} - e^{-j\tilde{k}L}}{j\tilde{k}}] \tag{5.11}$$

$$= 2K\frac{sin(\tilde{k}L)}{\tilde{k}L} \tag{5.12}$$

$$\frac{s_1(t)}{s_2(t)} = \frac{W_1(\tilde{k})}{W_2(\tilde{k})} \tag{5.13}$$

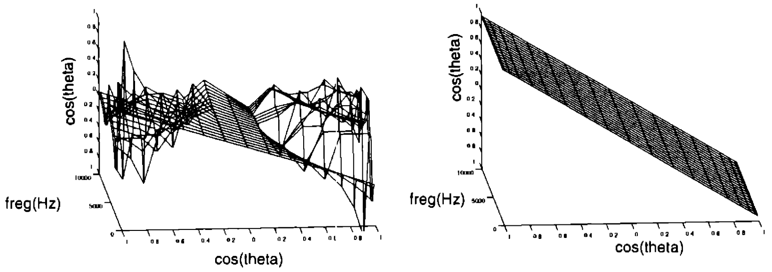

Figure 5-11: Plot of all data for untapered sensor

$$\frac{W_1}{W_2} = \frac{\frac{j4Ksin^2(\tilde{k}L/2)}{\tilde{k}}}{\frac{2Ksin(\tilde{k}L)}{\tilde{k}L}} \tag{5.14}$$

$$= \frac{j2sin^2(\tilde{k}L/2)}{Lsin(\tilde{k}L)} \tag{5.15}$$

The ratio in 5.14 cannot be made frequency independent with a simple integrator. However, for small $\tilde{k}$ – i.e. low frequency or angular proximity to the sensor's broadside – the squared sine cancels the denominator and can be approximated by the argument, $\tilde{k}L/2$, which in turn can be reduced to a dispersion-less ratio with a single-pole integration.

The surface plots for the untapered monopulse sensor's integrated, analytical ratio of Equation 5.14 are shown in Figure 5.2.3. As the figure shows, the surface of the untapered ratio is shaped similar to the dispersionless ratio's surface in $k - \tilde{s}pace$ for low frequencies and angles near broadside. Thus, one can think of the untapered sensor as a tapered sensor with shading errors (Equation 3.18) that are minimized within the main beam of the denominator.

The congregate plot of ratios formed for data acquired from the untapered sensor are shown in Figure 5.2.3, and the single frequency ratios are compared in Figure 5.2.3. The vertical and horizontal axes are similar to those for acquired data plots. Normalized slopes and offsets of the best fits for the data are compared to the tapered sensor's slopes and offsets in 5.2.3.

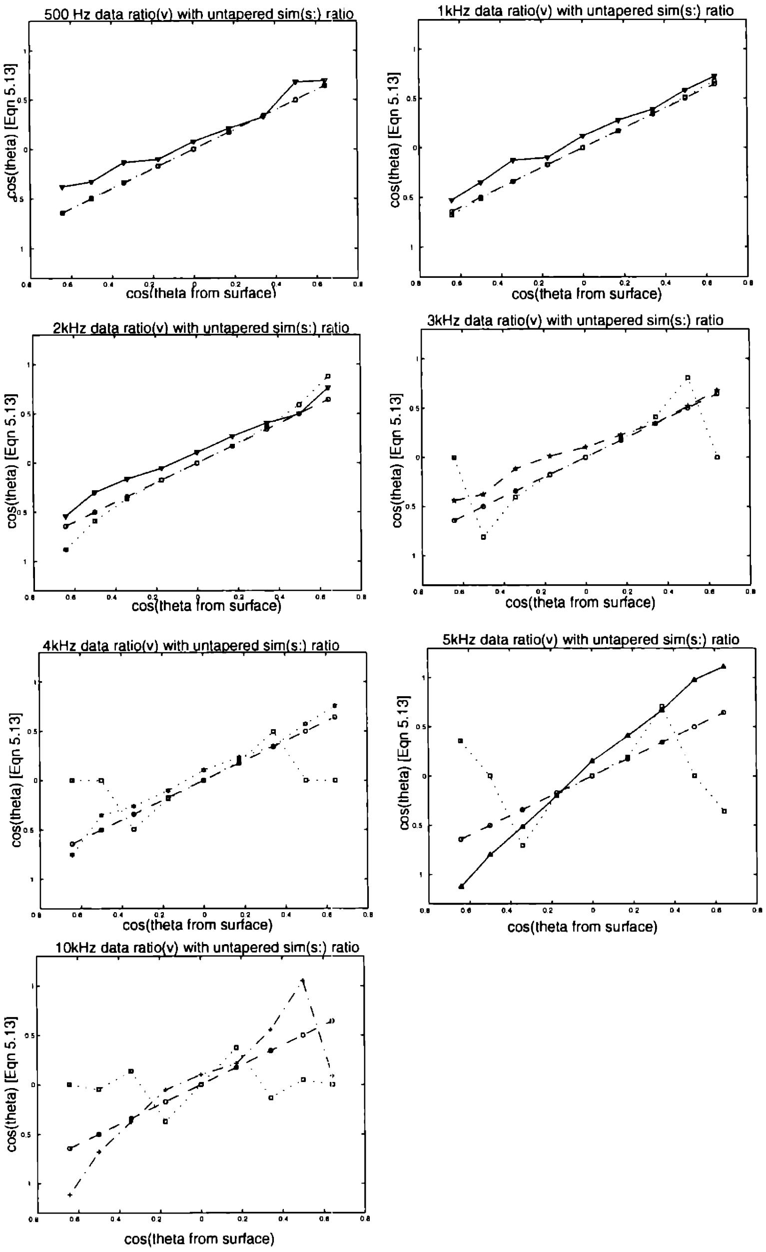

Figure 5-12: Plot of untapered sensor data, simulated untapered ratio, and ideal ratio

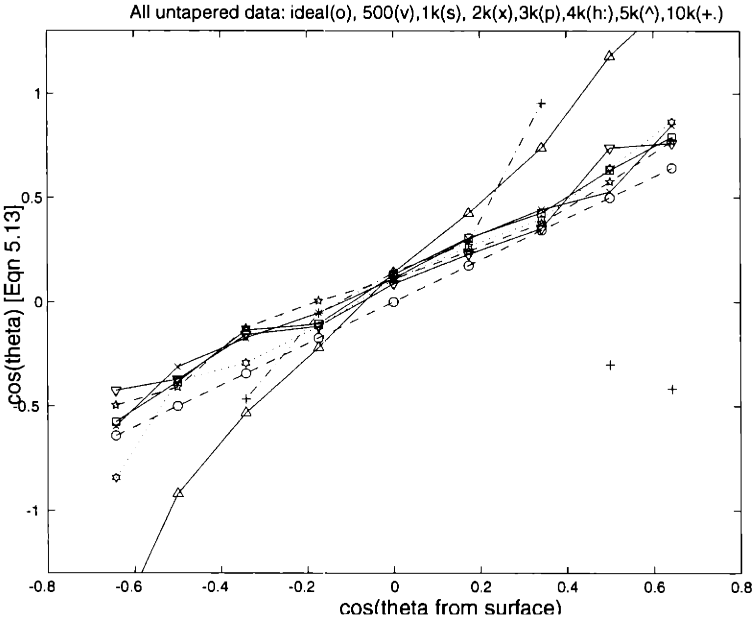

Figure 5-13: Plot of all data for untapered sensor

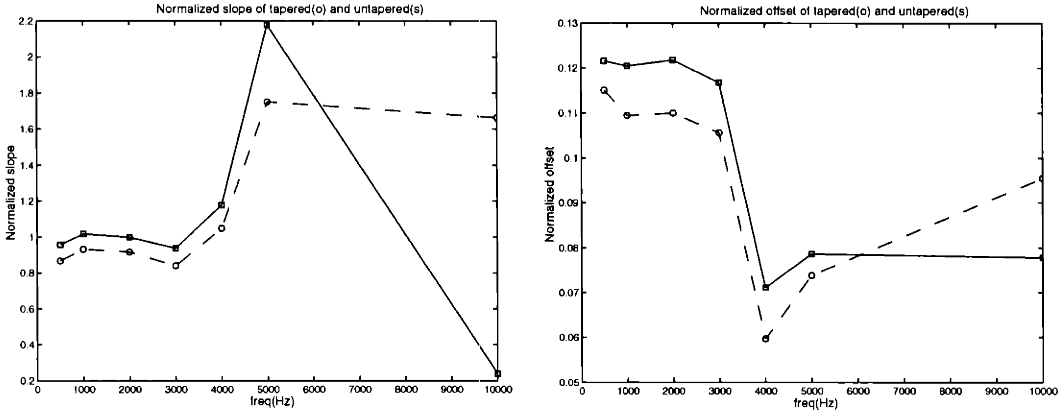

Figure 5-14: Normalized slope and offset for untapered aperture

5.2.4 Deconvolution data

An approach for correcting a non-ideal weighting and a non-ideal response due to the mounting was deconvolution. By first determining the weighting using a collimated source (to produce a line source), the actual weightings of the sensor, $W_1' = W_1 + E_1$ and $W_0' = W_0 + E_0$ could be found. A deconvolving filter $H(jw) = \frac{W_0}{W_0+E_3}$ could be used to correct the non-ideal ratio $\alpha(1 + \frac{E_3}{W_0})$. Unfortunately, a "line source" could not be easily constructed. Another method would be to use a transient-measurement system, such as MLSSA (DRA Laboratories, Sarasota, FL), to determine the weighting functions, with the source placed along the x-axis (0 degrees in Figure **??**). This, however, requires a bandwidth on the order of 50 kHz or more to obtain sufficient spatial resolution, which our sensor does not exhibit (Figure 5-2. Another possibility may be to measure the beam profile with high resolution and extract the wighting functions through the inverse transform to 3.2. Lacking the facilities to make such measurements, however, we have resorted to using the scanned image weightings shown in Figure 5-1.

Chapter 6

Conclusions and Future Directions

6.1 Conclusions

In this thesis, we have described the construction and operation of a monopulse device utilizing spatial shading to eliminate frequency dependence of the monopulse ratio. Signal processing was kept to a minimum, and direction estimates were restricted to reverberation-free time periods. Data was acquired and compared with the theoretical and simulated behavior of both tapered and untapered sensors. Feasibility for speech localization was also considered. The testing yielded several significant results:

- The sensor operates as a wideband monopulse sensor for a limited bandwidth ($\sim$ 4 kHz) over a limited angular range (at least 40°) in a normal laboratory room setting
- an untapered sensor works reasonably well in the voice band, as predicted by theory.
- The sensor performed best at low frequencies with the addition of a baffle.
- The sensor operates as a monopulse sensor for abrupt, non-voice cues of adequate amplitudes and, due to the difficulty in isolating first arrivals of voice cues, the sensor is not very useful for localizing voice sources.

- Because of the discrepancy between our simulated and acquired data for the tapered (derivative-matched) sensor, we do not fully understand how the hexcell support affects the shading of the PVDF foil.

6.2 Future directions

As in most investigations, the current investigation raised more questions than it answered. However, several directions which immediately suggest themselves from the findings of this thesis include the following:

- We must determine or understand the effects of the hexcell support on the acoustic response of the PVDF. Knowing the effects will allow us to implement and test knew shadings on hexcell support or to evaluate other possible supports.
- Once we determine the effects of the hexcell support – i.e., we know the effective shading that is realized on the hexcell – we can perform a deconvolution on a received signal with the known shading to recover the sensor's incident pressure signal
- Other techniques for robust ratio calculation can also be explored, including prefiltering to reduce noise that results in angle offsets. Envelope detectors that rise quickly and decay slowly can be developed, allowing ratio estimates to closely track the input waveforms without suffering from the large variance associated with zeros in the denominator signal.
- To demonstrate the viability and simplicity of the monopulse device for localization, we could implement a simple, microcontroller-based unit suitable for widespread use that would provide source bearing with an electronic or mechanical means.

Appendix A

Schematics

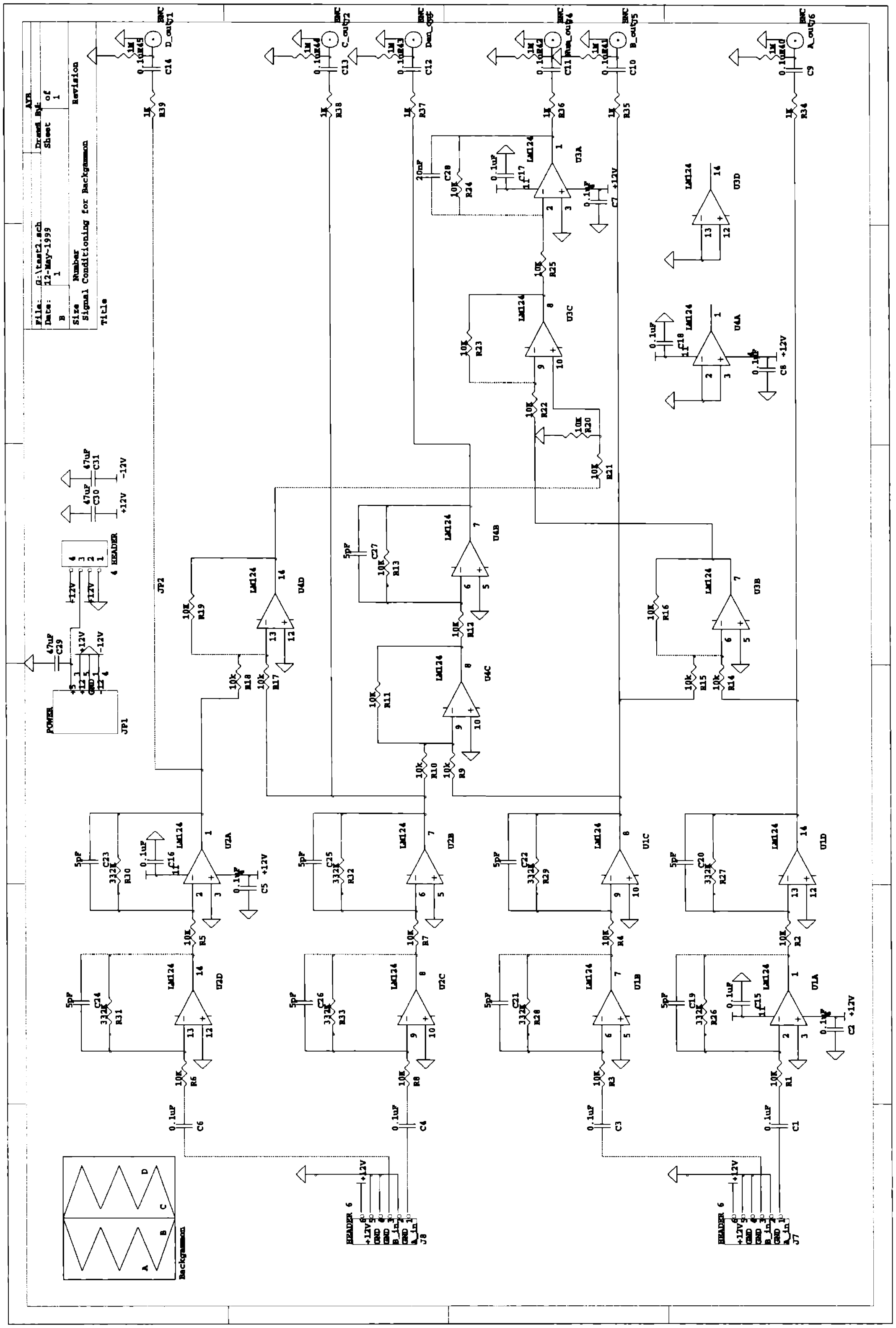

Figure A-1: Signal Conditioning Circuitry

Appendix B

Matlab scripts

B.1 Ratio estimator

```
path(path,'k:\'); path(path,'h:\'); path(path,'f:\');
path(path,'g:\'); path(path,'i:\'); path(path,'j:\');
 for pickfile= 0:6;
capdmeanarray =[]; capmeanarray =[];

capacitors = [330e-9; 75e-9;50e-9;33e-9; 20e-9; 10e-9];

for capacitorloop=1:6
    int_c   = capacitors(capacitorloop);
    switch pickfile
        case 0
         files = %% list of files for data files omitted here etc.
        case 1
            files = %% list of files for data files omitted here etc.
        case 2
            files = %% list of files for data files omitted here etc.
```

```
        case 3
            files = %% list of files for data files omitted here etc.
        case 4
            files = %% list of files for data files omitted here etc.
        case 5
            files =%% list of files for data files omitted here etc.
        case 6
            %% list of files for data files omitted here etc.
        otherwise
    end

sgn= []; mmratarray= []; mmdratarray = []; cossideangle = [];
cossideanglearray= [];
int_r1  = 10e3; int_r2  = 10e3; omega_c=
10/(int_r2*int_c); freq_c  = omega_c/(2*pi);

% For envelope detector, r=1600, c = 0.1e-6 ==> cutoff ~
%1000Hz lowpass
env_r = 6000;           %1600;
env_c = 0.12e-6;        %0.1e-6;
env_cutoffHz = 1/(2*pi*env_r*env_c);
% Overall
Td = 1/(60000);

% alpha is constant by which direction cosine is related
%to the ratio of the two signals

alpha1      = Td/(2*int_r1*int_c); alpha2      =
```

```
Td/(2*int_r2*int_c); betatop     =
alpha1*omega_c/sound*abs(1+exp(-j*omega_c*Td)); betabot     =
abs((alpha2+1) + (alpha2 -1)*exp(-j*omega_c*Td)); beta
= betatop/betabot;

filelength=9;

for   g = 1:filelength;%:2%length(file(1,:))

   load (files(g,:));
   data = truncated;

    A = data(:,1);
   B = data(:,2);
   C = data(:,3);
   D = data(:,4);

   % quick fix of too long vector (30010 instead of 30000)
   A = A(1:60000);
   B = B(1:60000);
   C = C(1:60000);
   D = D(1:60000);

   den = B+C;
 %  den_scaled = B_scaled + C_scaled;
   diff = A + B - C - D;
 %  diff_scaled = A_scaled+B_scaled-C_scaled-D_scaled;
   num = [];
```

```
% num_scaled = [];
 lengthofpulse=6000;
 for i=1:10
  num = [num ; integrate(diff((1+6000*(i-1)):
      (i*lengthofpulse)),Td,int_c,int_r1,int_r2)];
 end
  e_diff =  [];
  e_num  =   [];
  e_den  =  [];
 for i=1:10
    e_diff= [e_diff; envelopedetect(diff((1+lengthofpulse*(i-1)):
      (i*lengthofpulse)),Td,env_c,env_r)];
    e_num  = [e_num ; envelopedetect(num((1+lengthofpulse*(i-1)):
      (i*lengthofpulse)),Td,env_c,env_r)];
    e_den = [e_den ; envelopedetect(den((1+lengthofpulse*(i-1)):
     (i*lengthofpulse)),Td,env_c,env_r)];
 end
 t = [];
 for i=1:10
  t = [t (1+lengthofpulse*(i-1)) (lengthofpulse*i)];
 end
 % these limits are the ones actually used to find means. we
 %do not want to use sound bite in reverb
 finalt = triggerlocations2(e_den, 'threshold', .04, 0.0033, .1, Td);
 %use .04 threshold for 4kHz and above
 %finalt = triggerlocations2(e_den, 'threshold',
 % .1, 0.01, .1, 1/60000);
 % corrects for triggerlocations2's window looking to
```

```
   %the left of the actual threshold point
   finalt = finalt + 550;


    sgn = 0;
   sgn          = num.*den./(abs(num).*abs(den));
   for i=1:length(sgn)
      if ((sgn(i)~=1)&(sgn(i) ~=-1))
         sgn(i) = 1;
      end
   end
   % three cases to correct, num,den = 00, x0, or 0x
   % a reasonable thing to do is assign all NaN's to 1
   mrat             = getratio2(sgn,e_num,e_den,finalt);
   mdrat            = getratio2(sgn,e_diff,e_den,finalt);
   mrat;
   mmrat = mean(mrat);
   mmdrat= mean(mdrat);
    %  mmrat_scaled = mean(mrat_scaled);
%  This plots successive ratios of different scans
   mmratarray                   = [mmratarray; mmrat];
   mmdratarray                  = [mmdratarray; mmdrat];
end   % end of all computations for finding angles


% end of loop for capacitorloop
capmeanarray    =    [capmeanarray, mmratarray]


capdmeanarray = [capdmeanarray, mmdratarray]
end  % end of capacitor loop
```

```
end % end of pickfile loop
```

B.2 getratio2()

```
function ratios = getratio(sgn,num,den,times);
continue = 1;

if(mod(length(times),2)==1 | length(times)==0)
   continue = 0;
end
% Check that array is monotonically increasing
for i=1:length(times)-1
   if(times(i) >= times(i+1))
      continue = 0;
      break;
   end
end
%
if(length(num) ~= length(den))
   continue = 0;
end
 times; if(times(length(times)) > length(num))
   if (times(length(times))<60011)
      times(length(times))=60000;
     else
     continue = 0;
```

```
   end
end
% Do it.
if(continue==0)
   ratios = 0;
else
   lenrat = length(times)/2;
   ratios = zeros(1,lenrat);
for i=1:lenrat
  ratios(i) = mean(sgn(times(2*i-1):times(2*i))
   .*num(times(2*i-1):times(2*i))./den(times(2*i-1):times(2*i)));
   end
end
```

B.3 triggerlocations2()

```
function t = triggerlocations(data,type,arg1,arg2,arg3,arg4)
    i = 1;
   tloc = 1; %current index in time arra

if strcmp(type,'threshold')
   % arg1-4 should be [Vt ton toff td] where Vt
   %is the treshold voltage,
   % ton is the width of the pulse in seconds, toff
   %is the amount of time
   % after a pulse to reject other pulses and td is
   %the time seperation between
   % indices.
```

```
   Vt = arg1;
   ton = arg2;
   toff = arg3;
   td = arg4;
   if (ton<td)|(Vt<0)
      t(tloc)= 0;
      return;
   end
   while i <= length(data)
      %Did we trigger?
      if abs(data(i)) > Vt
         %Make sure we get a full pulse
         if (i+floor(ton/td)) > length(data)
            return
         end
         t(tloc) = i -500;  % back up a little bit
         t(tloc+1) = i + floor(ton/td)-500;
         tloc=tloc+2;
         i = i + floor(toff/td);
      end
      %Inc i regardless of above result
      i=i+1;
   end
elseif strcmp(type,'33')
   i = 1;
   while i <= length(data)
      i=i+1;
   end
```

```
else
   t(tloc) = 0;
end
```

B.4 lowpass()

```
function Y = lowpass(X,K,alpha);
% Numerator coefficients
b = [K K];
% Denominator coefficients
a = [alpha+1 alpha-1];

Y = filter(b,a,X);
```

B.5 integrate()

```
function Y = integrate(X,Td,c,r1,r2)
% Mimics, in finite time, the actions of an
%analog integrator with
% input resistance r1, feedback resistance
%r2 and feedback capacitor c.
% Since this is discrete time, we also need
%the sampling period Td.
% Returns the vector Y, the result of X being
%passed through the above filter.

% transform for integrator is
%[-1/(c*r1)]/[s + (1/(r2*c))]
```

```
% use bilinear transformation into DTime ie.
%(2/Td) (1-z^-1)/(1+z^-1)
% thus, DT transform equivalent represented here =
%[(-Td/(r1*2c))(1+z^-1)]/[(1+(Td/(r2*2c))) +
   (-1+(Td/(r2*2c)))z^-1]

alpha = Td/(2*r2*c); K = -Td/(2*r1*c);

Y = lowpass(X,K,alpha);
```

B.6 Spatial transform Simulation

```
ratio  = [];
nratio  = [];
testa     = 0;
signala = 0;
signalb =
0;
signalc = 0;
signald = 0;
signala_array  =  [];
 signalb_array
=  [];
signalc_array  =  [];
signald_array  =  [];
theta      =   0;

thetaarray      = [];
```

```
 freq           = 1000*2*pi;
endofsimulation= 1000;
sound           = 344; % speed of sound in meters/sec.
Ts  =  1/30000;

a = imread('actualA.bmp','bmp');
b=imread('actualB.bmp','bmp');

c = imread('actualC.bmp','bmp');
d = imread('actualD.bmp','bmp');
a = a(:, 2:649);
b = b(:, 2:649);
c= c(:, 2:649);
d = d(:, 2:649);
white = imread('actualwhite.bmp','bmp');

stave = imread('ActualStave.bmp','bmp');
imshow(stave);
imshow(a);
imshow(b);
imshow(c);
imshow(d);
Tx = 0.0042 %   the 4.2 mm is for 18 steps from 0-75.6 mm.Tx
    = .076/651; %sampling rate in space .076 meters/651 pixels
    samples for half the sensor
Ty = .051/433; % 5.21cm/433 pixels from top to bottom of sensor
% shading arrays; equal to area for each increment in x
weighta = ((sum(a))); weightb = ((sum(b))); weightc = ((sum(c)));
```

```
weightd = ((sum(d))); weight1 = (weighta + weightb - weightc
-weightd); weight0 = (weightb + weightc); newweight1 = [];
newweight0 = []; for step =1:18
   newwlsum = 0;
   neww0sum = 0;
   for pixel=1:36
        newwlsum = newwlsum+weight1(:,36*(step-1)+pixel)
        neww0sum = neww0sum+weight0(:,36*(step-1)+pixel)
   end
   newweight1 = [newweight1, newwlsum/36]
    newweight0 = [newweight0, neww0sum/36]
end wlarray = Tx*Ty*(newweight1); w0array = Tx*Ty*(newweight0);
endofsimulation     = 2/500/Ts; endoffreq          = 22;
endoftheta          = 18; W1_thetafreq = []; W0_thetafreq = [];
for (freqloop=1:endoffreq)
    freq=500*freqloop*2*pi;
    freqHz=500*freqloop
      W1_theta = [];
      W0_theta = [];
   for (thetaloop=0:endoftheta)
        theta = 2*pi*10*thetaloop/360;
      thetadeg = thetaloop*10
    %  for t=0:endofsimulation
        signalw1=0;
        signalw0=0;
         %this is the spatial integration,
         %without respect for the time varying part
         for g=1:18
```

```
            signalw0  =  signalw0 + w0array(g)*
             (cos(freq/sound*cos(theta)*Tx*(g-10))
             + j*sin(freq/sound*cos(theta)*Tx*(g-10)));
            signalw1  =  signalw1 + w1array(g)*
             (cos(freq/sound*cos(theta)*Tx*(g-10))
             + j*sin(freq/sound*cos(theta)*Tx*(g-10)));
         end
        W0_theta  = [ W0_theta; signalw0 ];
       W1_theta  = [ W1_theta; signalw1 ];
    end
    W1_thetafreq = [W1_thetafreq, W1_theta]
    W0_thetafreq = [W0_thetafreq, W0_theta]
end
% increase the frequency now
W1_hex = W1_thetafreq W0_hex = W0_thetafreq save W1_hex W1_hex;
save W0_hex W0_hex;
```

B.7 Time simulation

```
% uses Weighting functions to compute the time signal
load W1_hex.mat; load W0_hex.mat; W1 = W1_hex; W0 = W0_hex; Ts =
1/60000; endoffreq = 22;
 endoftheta = 18;

endofsimulation = 2/500/(1/30000);
s0_tXthetaXfreq =
[zeros(endofsimulation+1,endoftheta+1, endoffreq)];
s1_tXthetaXfreq = [zeros(endofsimulation+1,endoftheta+1,
```

```
endoffreq)];

for freqloop=1:endoffreq
   freq = freqloop*500*2*pi;
   s0_tXtheta = [];
   s1_tXtheta = [];
   for thetaloop=0:endoftheta
      theta = thetaloop*10*pi/180;
      s1_treal = [];
      s0_treal = [];
      for t=0:endofsimulation
         s1 = (1/j)*W1(thetaloop+1,freqloop)*exp(j*freq*t*Ts);
         s0 = W0(thetaloop+1,freqloop)*exp(j*freq*t*Ts);
         s1real = real(s1);
         s0real = real(s0);
         s1_treal = [s1_treal; s1real];
          s0_treal = [s0_treal; s0real];
       end
      s1_tXtheta = [s1_tXtheta, s1_treal];
      s0_tXtheta = [s0_tXtheta, s0_treal];
   end
   s1_tXthetaXfreq(:,:,freqloop) = s1_tXtheta;
   s0_tXthetaXfreq(:,:,freqloop) = s0_tXtheta;
end s1_hexj= s1_tXthetaXfreq; s0_hexj= s0_tXthetaXfreq; save
s1_hexj s1_hexj; save s0_hexj s0_hexj; 'done'
```

Bibliography

[1] C. Beauducel and T. Gautier. Increased sensitivity piezoelectric hydrophones. US Patent No. 4,810,913, March 7 1989.

[2] L. Beranek. *Acoustics.* McGraw-Hill, New York, 1954.

[3] P. Bevington. *Data Reduction and Error Analysis for the Physical Sciences.* McGraw-Hill, New York, 1969.

[4] M. Brandstein. *A framework for speech source localization using sensor arrays.* PhD thesis, Brown University, 1995.

[5] W. S. Burdic. *Underwater Acoustic System Analysis.* Prentice-Hall, Englewood Cliffs, NJ, 1984.

[6] S. Burke. *Shape and Vibration Control of Distributed Parameter Systems – Extension of Multivariable Concepts Using Spatial Transforms.* PhD thesis, Massachusetts Institute of Technology, Department of Mechanical Engineering, 1989.

[7] S. Burke. Design measures for shading robustness. *Draper Laboratory Technical Memorandum*, ESC-91-7:1–17, Dec 1991.

[8] S. Burke. Hilbert transforms: Applications to wideband monopulse data reduction. *Draper Laboratory Technical Memorandum*, ESC-92-173, May 1992.

[9] S. Burke. Monopulse sensor performance characterization. *Draper Laboratory Technical Memorandum*, ETB-92-379, Nov 1992.

[10] S. Burke and J. Hubbard. Wideband, derivative-matched, continuous aperture acoustic transducer. US Patent No. 5,237,542, August 17 1993.

[11] S. Burke and Jr. J. Hubbard. Distributed transducers for structural measurement and control. *Control and Dynamic Systems*, 36:223–273, 1990.

[12] S. Burke and J. Paradiso. High-resolution piezopolymer acoustic bearing estimator. March 1996. To be presented at Second Technical Conference on Telecommunications Research and Development.

[13] S. Burke and P. Rosenstrach. High resolution monopulse piezopolymer sonar sensor. *Proceedings of the 1992 Symposium on Autonomous Underwater Vehicle Technology*, 1:209–213, 1992.

[14] T. Henderson. Matched-beam theory for unambiguous broadband direction finding. *Journal of the Acoustical Society of America*, 78(2):563–574, 1985.

[15] T. Henderson. Wide-band monopulse sonar: processor performance in the remote profiling application. *IEEE Journal of Oceanic Engineering*, 12(1):182–197, 1987.

[16] C. Kyriakakis, P. Tsakalides, and T. Holman. Surrounded by sound. *IEEE Signal Processing Magazine*, 16(1):55–66, 1999.

[17] K. Martin. A computational model of spatial hearing. Master's thesis, Massachusetts Institute of Technology, Department of Electrical Engineering and Computer Science, 1995.

[18] M. Omologo and P. Svaizer. Acoustic event localization using a crosspower-spectrum phase based technique. *Proceedings of the ICASSP-1995*, 23(3):200–222, 1995.

[19] J. Paradiso. Backgammon electronics: Past, present, and future. *Draper Laboratory Technical Memorandum*, EJC 91-1100, Oct 1991.

[20] J. A. Paradiso. The interactive balloon: Sensing, actuation, and behavior in a common object. *IBM Systems Journal*, 35(34):473–487, 1996.

[21] D. Rabinkin, R. Renomeron, A. Dahl, J. French, J. Flanagan, and M. Bianchi. A dsp implementation of source location using microphone arrays. *Proceedings of the SPIE*, 22(4):20–22, 1995.

[22] D. V. Rabinkin, R. J. Renomeron, J. C. French, and J. L. Flanagan. Estimation of wavefront arrival delay using the cross-power spectrum phase technique. 1996.

[23] R. Renomeron, D. Rabinkin, J. French, and J. Flanagan. Small-scale matched filter array processing for spatially selective sound capture. *Proceedings of the ICASSP-1994*, 23(6):30–52, 1995.

[24] A. Van Schyndel. Nortel internal technical memo. October 1998.

[25] S. Sherman. *Monopulse Principles and Techniques.* Artech House, Norwood, MA, 1984.

[26] E. Skudrzyk. *The Foundations of Acoustics.* Springer-Verlag, New York, 1971.

[27] J. Sullivan. *Distributed Transducer Design for the Active Control of Multidimensional Elastic Structures.* PhD thesis, Massachusetts Institute of Technology, Department of Mechanical Engineering, 1994.